Working title:

Voltage-gated Ca^{2+} and K^+ channel coupling regulates CA1 hippocampal synaptic filtering and spine excitability

Authors:

Jonathan G. Murphy[1], Jakob J. Gutzmann[1], Lin Lin[1], Jiahua Hu[1], Ronald S. Petralia[2], Ya-Xian Wang[2], and Dax A. Hoffman[1]

Affiliations:

[1]*Eunice Kennedy Shriver* National Institute of Child Health and Human Development and [2]Advanced Imaging Core, National Institute on Deafness and Other Communication Disorders, National Institutes of Health, Bethesda, MD

ABSTRACT

The transient voltage-gated K^+ current (I_A) mediated by Kv4.2 in CA1 hippocampal pyramidal neurons regulates dendritic excitability, synaptic plasticity, and learning. Here we report that Ca^{2+} entry mediated by the voltage-gated Ca^{2+} channel subunit Cav2.3 regulates Kv4.2 function in CA1 pyramidal neurons through Ca^{2+} binding auxiliary subunits known as K^+ channel interacting proteins (KChIPs). We characterized an interaction between Cav2.3 and Kv4.2 using immunofluorescence colocalization, coimmunoprecipitation, electron microscopy, FRAP, and FRET. We found that Ca^{2+}-entry via Cav2.3 increases Kv4.2-mediated whole-cell current due in part to an increase in Kv4.2 surface expression. In hippocampal neurons, pharmacological block of Cav2.3 reduced whole-cell I_A. We also found reduced I_A in Cav2.3 knockout mouse neurons with a loss of the dendritic I_A gradient. Furthermore, the Cav2.3-Kv4.2 complex was found to regulate the size of synaptic currents and spine Ca^{2+} transients. These results reveal an intermolecular Cav2.3-Kv4.2 complex impacting synaptic integration in CA1 hippocampal neurons.

INTRODUCTION

In neuronal dendrites, voltage-gated ion channels modulate the amplitude, propagation and integration of synaptic input. The voltage-gated K^+ channel subunit Kv4.2 is highly expressed in the dendrites of hippocampal CA1 pyramidal neurons where it assembles into tetrameric channels that conduct a subthreshold-activated transient outward K^+ current known as A-type current (I_A) (1-5). Dendritic I_A regulates neuronal excitability by opposing depolarization to filter synaptic input, dampen the magnitude of backpropagating action potentials (bAP), oppose dendritic plateau potentials, and limit the size of glutamate uncaging evoked spine Ca^{2+} entry (5-11). As a consequence, the primary A-type channel expressed in CA1 pyramidal neuron dendrites, Kv4.2, plays an active role in shaping propagation of synaptic input, hippocampal synaptic plasticity, and learning (5, 8, 12-18). Dysregulation of I_A has been reported in both animal models and human cases of Alzheimer's disease, epilepsy, and pain sensitization (19-26). A better understanding of the mechanisms underlying neuronal I_A would facilitate the identification of therapeutic targets.

The properties of neuronal I_A can only be recapitulated in heterologous systems by expression of auxiliary subunits known as K^+ channel interacting proteins (KChIPs) and dipeptidyl aminopeptidase-like proteins (DPPs), which have profound effects on Kv4 subunit expression, stability, and biophysical properties (27-30). KChIPs are small (188-285 aa) Ca^{2+}-binding proteins of the neuronal Ca^{2+} sensor (NCS) gene family expressed from four genes (*KCNIP1-4*). KChIPs are highly conserved in their globular core domain (~70%) that contains N and C lobules, each with two EF-hands (EF) surrounding a deep hydrophobic pocket that cradles the N-terminus of the Kv4 subunit (31-33). Like the other NCS proteins, KChIP EFs 2, 3 and 4 bind divalent metal ions whereas EF1 is degenerated such that it cannot (34). At physiological free Ca^{2+} concentrations in neurons, the Ca^{2+} occupancy at the three Ca^{2+}-binding EF-hands is unknown. However, dynamic Ca^{2+} binding in response to transient Ca^{2+} elevations during neuronal activity could provide a regulatory feedback mechanism onto Kv4 channels. Interestingly, Ca^{2+} binding to purified KChIP induces global structural changes throughout the protein that may regulate oligomerization and Kv4 interactions (35-39). The effects of Ca^{2+} on the Kv4-KChIP complex has been studied using EF-hand mutations or by altering intracellular free Ca^{2+} concentrations (27, 31, 40-42). However, while EF-hand mutations potently reduce KChIP regulation of Kv4 channel trafficking and function, they are likely to disrupt the tertiary structure of the protein independent of Ca^{2+} (43). Furthermore, patch clamp studies of Kv4 channel function in various neuronal and non-neuronal cell types by addition of intracellular free Ca^{2+} or Ca^{2+} chelators in the patch pipette

have been variable and difficult to interpret (41, 44-46). In a similar effort to test the role of elevated intracellular Ca^{2+} on Kv4-KChIP function, we recently reported an increase in Kv4.2 current density when intracellular free Ca^{2+} was clamped at ~10 μM using a low affinity Ca^{2+} chelator (HEDTA) in the patch pipette in HEK293T cell recordings (42). This effect was unique to a subset of KChIP isoforms suggesting that cell-type specific KChIP expression may be an under-appreciated aspect of Ca^{2+} regulation of Kv4-KChIP complexes.

In neurons, it is well known that Ca^{2+} activated K^+ channels (KCa) rely on voltage-gated Ca^{2+} entry to repolarize the plasma membrane (47). However, the canonically voltage-activated Kv4 channels have also been reported to be targets of voltage-gated Ca^{2+} channel (VGCC) regulation through KChIP auxiliary subunits. Cerebellar stellate cells, small inhibitory interneurons that modulate Purkinje cell output, express Kv4-mediated I_A that is regulated by Ca^{2+} entry through low-threshold T-type voltage-gated Ca^{2+} channels (Cav3). T-type channel block with the L- and T-type channel-selective drug mibefradil increases the availability of I_A at more negative membrane potentials (48, 49). This effect was blocked by intracellular dialysis of BAPTA or pan-KChIP antibody consistent with a Kv4, Cav3, and KChIP complex.

In hippocampal CA1 pyramidal neurons, Wang and colleagues reported that Cav2.3 (R-type) voltage-gated Ca^{2+} channels function to attenuate the size of evoked EPSPs by boosting Kv4 channel function (50). Cav2.3 channels are expressed in the dendrites and spines of CA1 hippocampal pyramidal neurons and regulate action potential afterhyperpolarization and afterdepolarization, the magnitude of bAP evoked Ca^{2+} transients, and Ca^{2+} influx in spines and dendrites (51-57). Wang et al. disrupted Cav2.3 regulation of Kv4 using BAPTA or a pan-KChIP antibody in the patch pipette suggesting Cav2.3, Kv4, and KChIP are in close proximity (<50 nm). However, the studies by Wang and colleagues did not describe the nature of the Cav2.3-Kv4 interaction, nor the effect of Cav2.3-mediated Ca^{2+} entry on I_A. In the current study we corroborate and expand on the findings of Wang et al. by identifying a nanoscale interaction between Cav2.3 and Kv4.2 that regulates Kv4.2 function by a novel mechanism.

RESULTS

Cav2.3 and Kv4.2 form an ion channel complex in hippocampal neurons

The characteristic kinetics of neuronal I_A requires expression of KChIP and DPP accessory subunits that had been identified and described nearly two decades ago (27, 28). In an effort to identify novel Kv4.2 protein interactions and modifying enzymes in hippocampal neurons we used tandem affinity purification (TAP) and protein identification with mass spectrometry (MS) (58). As expected, Kv4.2 pulled down Kv4.1, Kv4.2, Kv4.3, and previously described auxiliary subunits (DPPs and KChIPs) confirming the specificity of the assay (**Figure 1 – Figure supplement 1A**). In addition to known binding partners, we also identified peptides representing a significant proportion of the Cav2.3 amino acid sequence (**Figure 1 – Figure supplement 1B,C**). Cav2.3 was the only voltage-gated Ca^{2+} channel identified in this screen.

To confirm the presence of a hippocampal Cav2.3 and Kv4.2 molecular complex we carried out several immunological measurements using hippocampal tissue. Broad neuropil colocalization of endogenous Cav2.3 and Kv4.2 immunofluorescent signal was consistent with enrichment in the dendrite layers of the hippocampus as has been previously reported for each channel separately (**Figure 1A**) (51, 59). Both Cav2.3 and Kv4.2 are also known to be expressed in dendrites and spines. To evaluate Cav2.3-Kv4.2 colocalization, we transfected cultured hippocampal neurons with Cav2.3-GFP (i), Kv4.2-myc (ii), and mCherry (iii) plasmids (**Figure 1B**). In addition to immunofluorescent colocalization in dendrites, both channels were enriched in spines when compared to the free cytosolic mCherry fluorescent protein (**Figure 1C,D**). Immunofluorescent overlap suggests that Cav2.3-Kv4.2 complexes may exist in dendritic spines, but, due to a lack of clear punctate signal we measured colocalization with greater precision using double immunogold electron microscopy. Gold particle labeling of Cav2.3 and Kv4.2 is visible near synapses in dendritic spines and we found evidence of colocalization both near the post synaptic density (**Figure 1Ei**) and in the spine head (**Figure 1Eii**). We further confirmed the Cav2.3-Kv4.2 complex by co-immunoprecipitation of native Kv4.2 after Cav2.3 pulldown in lysates from WT hippocampal tissue, but not Cav2.3 knockout (KO), confirming the specificity of the anti-Cav2.3 antibody (**Figure 1F**).

Cav2.3 regulates Kv4.2 mobility in HEK293FT cells and neuronal dendrites

If Cav2.3 and Kv4.2 bind, we reasoned that assembly of such a high molecular weight plasma membrane complex would result in a decrease in FRAP mobility. HEK293FT cells were transfected with either YFP-Cav2.3 and CFP or Kv4.2-CFP and YFP and photobleaching was

performed in separate cells (**Figure 2A**). When expressed separately, YFP-Cav2.3 mobile fraction (66.49 ± 0.01%) was considerably larger than Kv4.2-CFP (56.01 ± 0.09%) (**Figure 2B,E**). Expression of YFP-Cav2.3 and Kv4.2-CFP in the same cell and simultaneous bleaching yielded a decrease in mobile fraction for both YFP-Cav2.3 (56.28 ± 0.22%) and Kv4.2-CFP (36.77 ± 0.12%) suggesting that coexpression of Cav2.3 and Kv4.2 is sufficient to mediate a binding interaction in non-neuronal cells (**Figure 2C,D,E**). In neurons, prominent immunolabel colocalization led us to test whether Cav2.3 regulates Kv4.2 mobility in spines and dendrites. Primary mouse neurons cultured from either WT or Cav2.3 KO mice were transfected with Kv4.2-GFP and mCherry as a cell-fill to track dendrite structure during photobleaching recovery time-courses for small sections of dendrite shafts or entire spines (**Figure 2F,H**). Kv4.2-GFP mobile fraction was significantly higher in dendrites (55.96 ± 0.01%) when compared to spines (45.00 ± 0.02%) (**Figure 2G,I,J**). This result is consistent with the diffusion limit imposed by the spine neck and previously reported Kv4.2 interactions with postsynaptic scaffold proteins including PSD95 (60, 61), SAP97 (62), and AKAP79/150 (63). Kv4.2-GFP mobile fraction was increased specifically in dendrite shafts (+9.85 ± 3.21%) as opposed to spines (+6.45 ± 3.21%) of Cav2.3 KO mouse neurons (**Figure 2G,I,J**). This is likely due to the higher concentration of immobile Kv4.2 binding partners in spines relative to dendrites that mask the effects of Cav2.3 binding. Our FRAP results in both HEK293FT cells and cultured hippocampal neurons supports the hypothesis that Cav2.3 and Kv4.2 form a protein complex that reduces free diffusion of Kv4.2 in living cells.

Cav2.3 and Kv4.2 bind at a 1:1 ion channel stoichiometry within a cellular nanodomain

After confirming a Cav2.3-Kv4.2 complex in hippocampal neurons, we next sought to determine if Cav2.3 and Kv4.2 were within close enough proximity to each other to form a functional Ca^{2+} nanodomain. FRET is a distance dependent physical process that involves the non-radiative transfer of energy from an electronically excited donor to a nearby acceptor fluorophore; FRET efficiency decays at the inverse sixth power of the distance between two molecules (64). Using the CFP and YFP donor/acceptor pair, FRET can only be detected when the distance between donor and acceptor is <10 nm (65). To determine if Kv4.2 and Cav2.3 were within this distance we first introduced Kv4.2-CFP or YFP-Cav2.3 into HEK293FT cells with soluble YFP or CFP respectively to confirm that FRET would not arise from non-specific protein-protein interactions in the cell (0.68 ±0.34% and 0.46 ± 0.21%) (**Figure 3A,B**). To establish the utility of our FRET system, we then coexpressed Kv4.2-YFP and KChIP3a-CFP, which, as expected, yielded a high FRET efficiency (11.22 ± 0.57%). Coexpression of Kv4.2-CFP and YFP-Cav2.3 also resulted in FRET (6.71 ± 0.39%), confirming that they bind within a 10 nm domain

(**Figure 3A,B**). Next, we sought to leverage the maximal FRET efficiencies obtained from donor or acceptor-focused measurements to determine the stoichiometry of the Cav2.3-Kv4.2 complex using the method of Ben-Johny and colleagues (66). This method relies on maximizing the FRET signal at either the donor ($FRET_{D,MAX}$) or acceptor ($FRET_{A,MAX}$) with saturating concentrations of free acceptors or donors. The stoichiometry of the FRET complex can be estimated based on the maximal efficiency of interacting acceptors and donors and expressed as the stoichiometry ratio ($FRET_{A,MAX}/FRET_{D,MAX}$). We validated this method in our hands by taking advantage of known stoichiometries of Kv4.2 binding with KChIP (1:1) and A-kinase anchoring protein 79 (AKAP79) binding with the regulatory subunit of protein kinase A, RIIα (1:2). After coexpressing varying ratios of Kv4.2-YFP and KChIP3a-CFP we measured similar maximum FRET efficiencies at both donor and acceptor ($FRET_{A,MAX}$: 15.98 $\pm$ 0.64%; $FRET_{D,MAX}$: 15.75 $\pm$ 0.79%) consistent with a 1:1 interaction (**Figure 3C,F,G**). For AKAP79-YFP and PKA-RII-CFP we measured maximum FRET efficiencies that were most consistent with the expected 1:2 stoichiometry ($FRET_{A,MAX}$: 13.28 $\pm$ 1.13%; $FRET_{D,MAX}$: 5.35 $\pm$ 0.26%) (**Figure 3D,F,G**). Determination of the stoichiometry of YFP-Cav2.3 and Kv4.2-CFP indicated that the FRET complex was most consistent with a 1:4 acceptor:donor ratio that would be expected for a complex containing a single YFP-Cav2.3 α1 subunit and a Kv4.2-CFP homotetrameric channel ($FRET_{A,MAX}$: 14.52 $\pm$ 1.14%; $FRET_{D,MAX}$: 3.43 $\pm$ 0.33%) (**Figure 3E,F,G**). The results from our FRET experiments confirm that Cav2.3 and Kv4.2 are in close enough proximity to form a functional Ca^{2+} nanodomain (67, 68).

Cav2.3 expression increases Kv4.2 current density in a KChIP- and Ca^{2+}-dependent manner in HEK293FT cells.

Cav2.3 and Kv4.2 binding led us to hypothesize that Cav2.3 may act as a local neuronal Ca^{2+} source for Kv4.2 that can elevate nanodomain Ca^{2+} concentrations in the μM range. We previously reported that ~10 μM intracellular free Ca^{2+} increased Kv4 current density when expressed with a subset of KChIP isoforms including KChIP2b, KChIP2c, and KChIP3a (42). To determine if Cav2.3 could serve as a Kv4.2 Ca^{2+} source, we expressed either Kv4.2 alone (**i**), Kv4.2 and KChIP2c (**ii**), or Kv4.2, KChIP2c, and Cav2.3 (**iii**) (**Figure 4A**). As we and others have previously described, KChIP2c increased Kv4.2 current density and slowed fast inactivation of the macroscopic current (**Figure 4B,C**). Interestingly, coexpression of Cav2.3 significantly elevated Kv4.2 current density (**Figure 4B,C**) without affecting other aspects of KChIP-dependent regulation of Kv4.2 including voltage-dependence of inactivation and recovery from inactivation (**Figure 4E,F**). We tested whether local Cav2.3-mediated Ca^{2+} influx led to increases Kv4.2

current by replacing EGTA in patch pipettes with intracellular solution containing the fast Ca^{2+} chelator BAPTA. BAPTA blocked Cav2.3 increases in Kv4.2 current density (**Figure 4B,C**) consistent with a nanodomain Ca^{2+} influx-mediated effect. Coexpression of a Ca^{2+}-dead KChIP2c mutant, in which the Ca^{2+}-coordinating aspartate residue in position 1 of EF-hands 2, 3, and 4 was mutated to alanine, reversed the Cav2.3 effect (**Figure 4C**). Taken together, Cav2.3 expression caused a KChIP-dependent increase in Kv4.2 current density and required local increases in free Ca^{2+}. As we observed no changes in Kv4.2 gating behavior by Cav2.3, the increase in Kv4.2 current density may be explained by a change in channel surface localization. To test this possibility, we transfected COS7 cells with Kv4.2 alone, Kv4.2 and Cav2.3, Kv4.2 and KChIP2c, or Kv4.2, Cav2.3, and KChIP. We then surface labeled Kv4.2 with cell-impermeable biotin and quantified the amount of surface Kv4.2 relative to total expression. Expression of Cav2.3 with Kv4.2 and KChIP led to a significant increase in surface localization when compared to Kv4.2 and KChIP alone (**Figure 4G,H**). The evidence provided so far suggests that when Cav2.3 and Kv4.2 assemble in an ion channel signaling complex, Cav2.3-mediated Ca^{2+} entry increases Kv4.2 surface localization in a KChIP-dependent manner.

Cav2.3 sustains I_A in cultured hippocampal neurons.

Armed with evidence that Cav2.3 and Kv4.2 colocalize in hippocampal neurons and that Cav2.3 regulated Kv4.2 surface levels in heterologous cells, we wanted to determine if Cav2.3-mediated Ca^{2+} entry regulates Kv4.2 function in neurons. The prominent dendritic localization of Kv4 channels obscures accurate measurement of I_A using voltage clamp recordings from the soma of developmentally mature neurons. However, at early developmental time points before dendrite outgrowth and synaptic maturation, Kv4 channels would be predicted to be better clamped (1). We found that somatic I_A density in cultured hippocampal neurons reaches a maximum at 6-8 days in vitro (**Figure 5 – Figure Supplement 1A**). As the cultures mature, I_A density drops dramatically as dendrites elaborate and excitatory synaptic development progresses (**Figure 5 – Figure Supplement 1A,B**). Peak Cav2.3 current is elicited at membrane potentials near 0 mV (69, 70). To maximize Cav2.3 channel activation we measured peak I_A in DIV6-8 cultured neurons using voltage steps from -80 mV to 0 mV. Under these conditions, the peak transient outward K^+ current was highly enriched for I_A relative to the slowly activating delayed rectifier K^+ current (92.49 $\pm$ 0.02%; data not shown); therefore, we monitored total peak outward current as a proxy for I_A. Voltage clamp recordings of I_A were stable over a 360 s recording period (**Figure 5Ai,B,C**). We confirmed the presence of Kv4 channels in I_A recordings by applying AmmTX3, a Kv4 selective scorpion toxin that requires the DPP auxiliary subunit for

high potency (**Figure 5Aii,B,C**) (71, 72). Ni^{2+}, a nonspecific VGCC blocker with high potency at T- and R-type channels was applied to determine the effect of Cav2.3 on I_A (70, 73). Application of Ni^{2+} to the bath led to a rapid dose-dependent reduction in I_A (**Figure 5Aiii,B,C,D**). IC_{50} of I_A block (~44.1 μM) was within the reported IC_{50} range of Cav2.3 block by Ni^{2+} (27.4-66.0 μM) (74). Ni^{2+} application did not shift I_A voltage dependence of inactivation as was previously reported for Cav3 regulation of I_A in cerebellar stellate neurons (**Figure 5E**) (48, 49).

I_A is reduced in Cav2.3 KO CA1 pyramidal neurons.

To overcome the limitations of VGCC pharmacology, we measured I_A in the context of a previously characterized Cav2.3 KO mouse (57, 75). Here, we made recordings from 6-8 weeks old mouse CA1 pyramidal neurons. Unlike the DIV6-8 neurons used above, these neurons are greater in size and express a more substantial proportion of contaminating delayed rectifier K^+ currents. Therefore, I_A was isolated as previously described using large voltage steps and subtraction of the sustained outward current (I_{sus}) from the total outward current (I_{tot}) (**Figure 6A**) (58). I_A was selectively reduced in whole-cell recordings from Cav2.3 KOs when compared to WT mouse neurons while I_{sus} was unchanged (**Figure 6B**). Given the previously mentioned complications with whole-cell voltage clamp, we pulled patches from the soma; however, outside-out patches did not replicate the whole-cell reduction in I_A (**Figure 6C**). One explanation would be if the whole-cell reduction in I_A we observed in Cav2.3 KO recordings arose from a specific loss of dendritic Kv4.2 channels. To determine this, we performed cell-attached dendritic recordings along the apical dendrite (**Figure 6D**). The results showed a significant decrease in the dendritic I_A gradient in Cav2.3 KO neurons (**Figure 6E**). These findings suggest that Cav2.3 channel expression is linked to maintenance of the magnitude of I_A in distal dendrites.

Cav2.3 channels promote I_A-mediated excitatory synaptic filtering.

Voltage-gated ion channels open in response to synaptic depolarization in excitatory synapses (9, 55, 76, 77). Therefore, the size of the synaptic current measured at the cell soma is not only the result of transmitter release and glutamate receptor function but also of active membrane properties. Kv4.2 and Cav2.3 channels are localized to CA1 spines and dendrites where they affect the synaptic potential and shape its propagation (5, 50, 51, 55, 78-80). We have previously shown that I_A reduces the magnitude of spontaneous miniature EPSCs (81). Therefore, if Cav2.3 channels boost I_A, Ni^{2+} would be expected to reduce I_A in spines and dendrites and enhance mEPSC propagation. To test this, we applied Ni^{2+} while holding cultured neurons at -70 mV and recorded AMPAR-mediated mEPSCs in the presence of voltage-gated Na^+ and GABAR

blockers (**Figure 7A**). Ni^{2+} caused a rightward shift in the cumulative distribution of mEPSC amplitudes, though with smaller effect than direct blockade of Kv4 with AmmTX3 (**Figure 7B**). Simultaneous application of Ni^{2+} and AmmTX3 to the bath mimicked AmmTX3 alone, suggesting that Kv4 channel block occluded any additive effect of Ni^{2+} on mEPSC amplitudes (**Figure 7B,C**). Despite an increase on postsynaptic currents, Ni^{2+} reduced mEPSC frequency consistent with the contribution of Ni^{2+}-sensitive presynaptic VGCCs to glutamate release in the hippocampus (**Figure 7D**) (50, 73, 82).

We next sought a method to investigate the local spatiotemporal effects of the Cav2.3-Kv4.2 complex on synaptic function. Fluorescent Ca^{2+} indicators are suited for visualization of NMDAR Ca^{2+} entry in response to spontaneous, quantal glutamate release (83-85). We transfected cultured hippocampal neurons with the genetically-encoded fluorescent Ca^{2+} indicator GCaMP6f along with mCherry to illuminate dendrite morphology. We imaged spontaneous NMDAR-mediated Ca^{2+} transients in Mg^{2+}-free extracellular solution containing TTX to block action potential backpropagation, which would obscure spontaneous quantal NMDAR-mediated Ca^{2+} entry. The frequency, amplitude, and duration of spontaneous Ca^{2+} transients were highly variable both among and within individual spines, with some spines being completely inactive during imaging trials (**Figure 8A**). The NMDAR blocker APV completely abolished Ca^{2+} transients consistent with a requirement for spontaneous glutamate release onto NMDARs to initiate Ca^{2+} influx (**Figure 8A,B**). Variability and low event frequency required identification of spines that were active both before and after pharmacological treatments. AmmTX3 block of Kv4 channels did not alter the amplitude of Ca^{2+} transients but did lengthen the event half-width suggesting that Kv4 channels oppose spine depolarization initiated by glutamate receptors (**Figure 8C**). Kv4 block increased the integrated amount of Ca^{2+} entry (**Figure 8D**). As expected, Ni^{2+} reduced integrated spine Ca^{2+} signals likely due to a combinatorial effect on Ni^{2+} sensitive pre- and postsynaptic VGCCs (**Figure 8E**). To determine if Cav2.3 Ca^{2+} entry modulated the function of Kv4 channels, we applied Ni^{2+} followed by addition of AmmTX3. Preapplication of Ni^{2+} occluded the AmmTX3-induced increase of spine Ca^{2+} suggesting Cav2.3-mediated Ca^{2+} entry is required to maintain spine repolarization by Kv4 channels (**Figure 8F**).

DISCUSSION

The present study was designed to both confirm and define the nature of a Cav2.3-Kv4.2 complex identified from a proteomic screen and to assess its functional consequences in CA1 pyramidal neurons. We show here that Cav2.3 and Kv4.2 colocalize within dendritic spines of CA1 pyramidal neurons, likely within a 10 nm nanodomain at 1:1 stoichiometry as shown by FRET microscopy in HEK293FT cells (**Figures 1,2**). Functionally, we found that the Cav2.3-Kv4.2 interaction increases Kv4.2 surface localization and contributes to maintenance of the dendritic gradient of I_A in CA1 pyramidal neurons (**Figures 3-6**). Previous studies have demonstrated that dendritic I_A regulates excitability, spine Ca^{2+} entry, back propagation of action potentials, plateau potentials, synaptic plasticity, and hippocampus-dependent learning (86-88). In regulating the magnitude of I_A as shown here, the Cav2.3-Kv4.2 complex therefore plays a fundamental role in dendritic function. Consequently, Cav2.3-mediated Ca^{2+} entry would be expected to support the many roles of dendritic I_A. Indeed, we found that Ni^{2+} occluded AmmTX3-mediated boosting of spine Ca^{2+} signals and increased the amplitude of AMPAR-mediated mEPSCs (**Figures 7,8**).

Here we have corroborated and expanded upon the studies of Wang and colleagues who first described a Kv4 and R-type Ca^{2+} channel functional interaction at CA1 synapses (50). They demonstrated that block of R-type VGCCs using SNX-482 increased the amplitude of Schaffer collateral evoked EPSPs. This effect was occluded by Kv4 block using the non-selective voltage-gated K^+ channel blocker 4-AP, expression of a dominant negative Kv4.2 (W362F) subunit, or KChIP sequestration with a pan-KChIP antibody in the patch pipette. Furthermore, internal 10 mM BAPTA occluded the effect of SNX-482, which, together with the reliance on KChIPs, provided evidence for a small intermolecular distance (≤ 50 μm) between the Ca^{2+} source and the putative Kv4 channels. One potential criticism of this work was the reliance on SNX-482, which, shortly thereafter, was found to be a potent Kv4 blocker with an IC_{50} ~10-fold greater for Kv4.3 than Cav2.3 (89, 90). However, SNX-482 inhibition of the predominant CA1 isoform, Kv4.2 is much less pronounced and the EPSP boosting effect was repeated using Ni^{2+}, an alternative VGCC blocker (50). Most importantly, the SNX-482 effect could not be reproduced in Cav2.3 KO mice (79). Together with the evidence presented here, there is a strong argument that the SNX-482 effects observed in the Wang et al studies were likely due to VGCC block and not off target effects at Kv4 channels.

Here we describe a novel connection between the Cav2.3 and Kv4.2 pore-forming subunits functionally impacting synaptic integration. Cav2.3 and Kv4.2 double immunogold labeling was not seen within the PSD (**Figure 1E**), rather complexes were localized to peri- or

extrasynaptic domains in spines as described previously (51, 81). Furthermore, we found that heterologously expressed Cav2.3 and Kv4.2, in the absence of coexpressed auxiliary subunits, form a nanodomain signaling complex using C-YFP FRET microscopy (**Figure 3**). FRET can only be measured when C- and YFP are within 10 nm and we estimate the diameter of the Kv4-KChIP complex itself to be close to ~10 nm based on the Kv2.1-β_2 channel structure (91). Therefore, KChIPs arrayed around the intracellular T1 domain of the Kv4.2 channel could be exposed to Ca^{2+} concentrations approaching 10 μM during Cav2.3 channel openings based on Ca^{2+} source diffusion models (68). While the steady-state Ca^{2+} occupancy of KChIP is unknown *in vivo*, dynamic KChIP Ca^{2+} binding is a compelling mechanism that may account for Cav2.3-mediated regulation of Kv4.2 surface expression through reduced channel turnover. In a test tube, Ca^{2+} binds to KChIP at high (EF3 and EF4) and low affinity sites (EF2, preferring Mg^{2+} over Ca^{2+}) and Ca^{2+} binding plays a critical role in KChIP folding and binding to Kv4 channels (31, 36, 37, 43). In reported structures, only EF3 and EF4 of KChIP1 are Ca^{2+}-bound, whereas it has been hypothesized that EF2 distortion by Kv4.3 N-terminal binding renders it unable to accommodate Ca^{2+} (31, 92, 93). While these studies are informative there remains a relative dearth of mechanistic detail for Ca^{2+} regulation of endogenous Kv4-KChIP complexes involving full length proteins and functional channels. While an *in vivo* mechanism for dynamic KChIP-Ca^{2+} exchange remains elusive, KChIP binds Ca^{2+} in the μM range, suggesting local Ca^{2+} elevations may induce KChIP structural rearrangements that promote Kv4.2 surface expression.

To our knowledge, the contribution of voltage-gated channels to quantal NMDAR-mediated Ca^{2+} signals is unprecedented. In prior studies, pharmacological block of either AMPAR or voltage-gated channels had no measurable effect on quantal NMDAR-mediated Ca^{2+} transients (94, 95). However, subthreshold synaptic depolarizations can activate voltage-gated channels including R-, T-type, and A-type channels (5, 9, 55, 76, 77). Why did prior studies not find a contribution of voltage-gated channels to the quantal NMDAR-mediated Ca^{2+} signals? We found that if our data were treated similarly, by measuring the mean amplitudes across spines before and after treatments, the large variability both between and among spines obscured any effect of pharmacological manipulation of voltage-gated channels (data not shown). The effects of pharmacological treatments were only apparent through repeated imaging of specific spines before and after treatments. We also found that Kv4 channels in particular, regulated the duration of spine Ca^{2+} events more so than amplitude, necessitating comparison of Ca^{2+} signal integrals. A presynaptic effect of Ni^{2+} and/or AmmTX3 on neurotransmitter release might also produce the changes in spine Ca^{2+} signals we observed. To address this, we recorded AMPAR-mediated mEPSCs, and application of Ni^{2+} increased mEPSC amplitude despite a reduction in frequency.

Conversely, AmmTX3 increased amplitude and did not affect mEPSC frequency consistent with prior studies that have ruled out a presynaptic role for Kv4.2 channels (50, 96).

In the present study, we report measurements of I_A in cultured neurons and hippocampal slices to provide strong evidence for regulation of the magnitude of I_A by Cav2.3 channels. Cav2.3-mediated Ca^{2+} entry was sufficient to increase Kv4.2 functional expression in a KChIP-dependent manner in non-neuronal cells. We also show Cav2.3 regulation of neuronal I_A using VGCC pharmacology and Cav2.3 KO mice. Several lines of evidence support a Cav2.3-mediated Ca^{2+}- and KChIP-dependent trafficking mechanism as opposed to regulation of Kv4.2 conductance or gating in CA1 pyramidal neurons. First, increased single channel conductance has ostensibly been ruled out as a mechanism for the increase in Kv4 current density mediated by KChIPs (97, 98). However, it is yet to be determined if elevations of intracellular Ca^{2+} may regulate Kv4 single channel conductance. Second, we reported previously that elevated intracellular Ca^{2+} led to an increase in Kv4 current density without affecting classical KChIP-dependent processes including inactivation gating (42). However, stoichiometric KChIP binding is expression dependent (99-101) and we should point out here that if Ca^{2+} caused shifts in Kv4 binding affinity for KChIP this likely would be overcome by the significant overexpression of KChIP relative to Kv4 in those studies (~8:1 molar excess). Lastly, our surface biotinylation experiments shown here demonstrate increased Kv4.2 surface localization by Cav2.3 coexpression, again without changes in channel gating consistent with our previous report. Taken together, Cav2.3-Kv4 functional coupling in CA1 pyramidal neurons primarily increases the magnitude of Kv4.2 currents through enhanced surface expression or stability. This is in contrast to the mechanism demonstrated for the Cav3-Kv4 channel complex in cerebellar interneurons which results in enhanced I_A via a shift in channel availability to more negative potentials (48, 49). It remains to be determined what mediates the disparate regulatory mechanisms in CA1 pyramidal neurons and cerebellar stellate cells.

I_A increases linearly ~5-fold on the distal apical dendrites 350 μm from the soma of CA1 pyramidal neurons (5). Curiously, histochemical measurements of Kv4.2 expression levels suggest at most a 2-fold increase in expression along the proximal-distal extent of the stratum radiatum (1, 59, 78, 102). A constellation of studies supports both auxiliary subunit and enzyme-dependent pathways may underlie the disparity between Kv4.2 expression and function. The DPP6 auxiliary subunit establishes the Kv4.2 functional gradient in CA1 pyramidal neurons through enhanced surface expression, a shifted voltage-dependence of activation to more hyperpolarized potentials, and while the mechanistic basis for this is still unclear, DPP6 clearly mediates dendrite directed Kv4.2 trafficking and function in distal dendrites (15). Distal dendritic I_A activates at more negative membrane potentials when compared to proximal or somatic I_A (5),

and this is reversed by activity of PKA, protein kinase C (PKC), or mitogen activated kinase pathways (12, 103, 104). During induction of synaptic plasticity, Kv4.2 channels internalize in an NMDAR- and Ca^{2+}-dependent manner by PKA phosphorylation at Ser522 (61, 81). Furthermore, Kv4.2 surface expression is bidirectionally regulated by local signaling of the Ca^{2+}-activated phosphatase calcineurin (CaN) and PKA through the postsynaptic scaffolding protein AKAP79/150 (63). We recently reported a role for a proline isomerase, Pin1 in activity-dependent downregulation of Kv4.2 function downstream of p38 phosphorylation of T607 (58). Thus, differential localization of kinases and phosphatases along the proximal-distal axis of CA1 pyramidal neurons could underlie the I_A gradient and is an important topic for further study. It is possible that Cav2.3 Ca^{2+} entry may impinge on these pathways in a Ca^{2+}-nanodomain fashion. For example, AKAP79/150 localizes PKA and CaN for phospho-regulation of AMPAR and L-type Ca^{2+} channels (105). Hypothetically, Cav2.3 Ca^{2+} entry could also drive activation of AKAP-anchored CaN and dephosphorylate Kv4.2 channels, favoring surface expression. Finding the mechanistic link between local Ca^{2+} influx and increased Kv4.2 surface expression is a goal for future research.

KChIP heterogeneity is a largely unexplored area of research in CA1 pyramidal neurons. Alternative splicing and variable start codons of the *KCNIP1-4* transcripts result in up to 17 distinct KChIP isoforms with unique N-terminal domains. Variant KChIPs have been categorized based on the tendency for the N-terminus to mediate membrane interactions (33). A subset of "cytoplasmic" KChIP isoforms confer Ca^{2+} regulation onto Kv4.2 channel complexes, N-myristoylated isoforms do not, and reversibly palmitoylated isoforms have mixed Ca^{2+} sensitivity (42). Members of a fourth transmembrane class of KChIPs retain Kv4.2 complexes within the ER and reduce Kv4.2 surface expression when compared with other KChIP isoforms (106). In hippocampus, there is overlapping expression of both Ca^{2+} sensitive and Ca^{2+} insensitive KChIP isoforms. Could differential subcellular targeting of KChIPs lead to increased Kv4.2 function in distal dendrites? Perhaps membrane-anchored KChIPs, like the Kv4.2 suppressor KChIP4a, may be restricted to soma and proximal dendrites. *KCNIP1-4* mRNAs have been detected in the CA1 neuropil, suggesting they may be locally translated (107, 108). Dendrite targeted *KCNIP* mRNAs may also undergo alternative splicing for conditional or spatiotemporal modification of Kv4.2 function. In fact, a KChIP4bL to KChIP4a splicing shift occurs in postmortem brain tissue isolated from Alzheimer's patients resulting in reduced functional I_A (109). It is also possible that KChIPs may confer Ca^{2+} regulation to Kv4 channel complexes through a mechanism unrelated to direct KChIP-Ca^{2+} binding. KChIP assembly with Kv4.2 is required for downregulation of Kv4.2 surface expression in response to PKA Ser552 phosphorylation (110). Additionally, reduced Kv4 function

by arachidonic acid is also mediated by assembly with KChIPs (111). Thus, there may be ultrastructural roles of KChIPs that augment Kv4.2 in such a way as to affect sensitivity to various forms of regulation.

The majority of CA1 dendritic I_A is mediated by Kv4.2 subunits, ruling out a significant contribution of other A-type channels that include Kv1 and Kv4 subtypes (13). Here, we show that the functional I_A gradient is disrupted in the Cav2.3 KO mouse (**Figure 6D,E**). Others too have found that Ni^{2+} sensitive VGCCs are a significant source of Ca^{2+} in dendrites and spines (9, 55, 76, 77). One compelling hypothesis, given the results presented here, is that tonic Cav2.3 activity in distal dendrites sustains Kv4.2 functional expression. The increasing distal dendritic gradient of Kv4.2 expression correlates with the ratio of excitatory and inhibitory synapses along the apical dendrite layers of the hippocampus (112, 113). Therefore, ongoing low-level spontaneous excitatory synaptic transmission and Cav2.3-mediated Ca^{2+} entry may maintain Kv4.2 expression as a homeostatic mechanism to regulate local dendritic excitability. This mechanism could be overridden by LTP-stimulated endocytosis of Kv4.2 driven by strong synaptic input in an NMDAR-dependent mechanism like we have previously described (61, 81). This would fit with the reported increase in excitability of dendritic segments containing potentiated synapses following Shaffer Collateral-CA1 LTP (88). The findings reported here open up several avenues of research into the function of the Cav2.3-Kv4.2 complex in dendrite function and plasticity; however, a lack of Cav2.3 specific pharmacology without overlapping effects at Kv4 channels makes this work more challenging. Future studies aimed toward identifying Cav2.3-Kv4.2 interaction domains could be leveraged to disrupt the complex. This would be of significant utility to isolate functions unique to the Cav2.3-Kv4.2 complex as opposed to their independent roles in the hippocampus.

475 MATERIALS AND METHODS

476

477 **Mammalian expression vectors**

478 Cav2.3-GFP was a generous gift from Ehud Isacoff, University of California Berkeley (114). The
479 SGFP2-N1 plasmid was generated by replacement of YFP in YFP-N1 using AgeI/BsrGI sites to
480 excise SGFP2 from pSGFP2-C1 (Dorus Gadella, Addgene 22881 (115)). Kv4.2-CFP, Kv4.2-YFP,
481 and Kv4.2-SGFP2 fusions were created by ligating the mouse Kv4.2 (CCDS29974.1) from Kv4.2-
482 GFP (81) into the CFP-N1 vector using SalI/BglII sites. YFP-Cav2.3 was generated by PCR
483 amplification of the human Cav2.3 (CCDS55664.1) coding sequence from Cav2.3-GFP using
484 BglII/HindIII sites for ligation into the YFP-C1 vector (performed by Bioinnovatise, Inc). Rat pCMV-
485 KChIP2c was generously provided by Henry Jerng and Paul Pfaffinger, Baylor College of
486 Medicine, Houston, TX. Ca^{2+}-dead KChIP2c was generated by site directed mutagenesis using
487 D->A mutations at position 1 of each of EF2,3, and 4 (Stratagene, QuikChange Site-Directed
488 Mutagenesis Kit). KChIP2c-CFP was generated by PCR amplification of the rat KChIP2c ORF
489 (NM_001033961.1) from pCMV-KChIP2c and subcloned into CFP-N1 using BglII/SalI sites.
490 AKAP79-YFP and PKARII-CFP were gifts from Mark L. Dell'Acqua, University of Colorado School
491 of Medicine, Aurora, CO. The CFP-18aa-YFP tandem fusion construct used for FRET efficiency
492 calibrations was a gift from Clemens Kaminski (University of Cambridge). GCaMP6f was a gift
493 from Douglas Kim & GENIE project (Addgene 40755 (116)). Human Kv4.2-Myc-DDK (Origene,
494 RC215266), ECFP-N1, EYFP-C1, EYFP-N1, and mCherry-N1 are commercially available
495 (Takara Bio).

496

497 **Antibodies**

498 *Guinea pig anti-Cav2.3* was a generous gift from Akos Kulik, University of Freiburg (51), 1:100 for
499 EM; 1:1000 for IHC; 1:5000 for WB. *Mouse anti-Kv4.2* (K57/1): NeuroMab 75-016, 1:25 for EM;
500 1:300 for IHC; 1:2000 for WB. *Mouse anti-Myc*, Millipore 05-419, 1:500 for ICC. *Alexa Fluor 488*
501 *goat anti-guinea pig*: ThermoFisher A11073, 1:800 for IHC. *Alexa Fluor 488 goat anti-rabbit*:
502 ThermoFisher A11008, 1:500 for ICC. *Alexa Fluor 555 goat anti-mouse*: ThermoFisher A21422,
503 1:800 for IHC. *Alexa Fluor 647 goat anti-mouse*: ThermoFisher A21236, 1:500 for ICC. *Alexa*
504 *Fluor 680 goat anti-mouse*: ThermoFisher A21057, 1:10,000 for WB. *IRDye 800CW goat anti-*
505 *rabbit*: Li-Cor Biosciences 926-32211, 1:5,000 for WB. *Rabbit anti-GFP*, ThermoFisher A11122,
506 1:500 for ICC; 1:3000 for WB

507

508 **Cell culture**

HEK293FT and COS7 cells were maintained in DMEM supplemented with 10% fetal bovine serum (ThermoFisher, A3160501) and 2% penicillin/streptomycin (ThermoFisher, 15140122) at 37°C and 5.0% CO_2. Cells were passaged 2x weekly by seeding 0.5-1.0 x 10^6 cells into 10 cm culture dishes (Corning). Cell lines were kept up to passage 20.

Humane rodent care and use

All protocols and procedures were approved by the National Institute for Child Health and Human Development Animal Care and Use Committee. All mice were housed and bred in the Porter Neuroscience Research Center animal facility at the National Institutes of Health in Bethesda, MD. Rodents were maintained on a 12 h light/dark cycle with *ad libitum* access to rodent chow and water. Cav2.3 KO mice used for hippocampal cultures and brain slice electrophysiology were generously provided by Dr. Richard Miller, Northwestern University (75). Cav2.3 KOs were maintained on a C57Bl/6J background. Age-matched wild-type C57Bl/6J mice (WT) were used as controls. Rat hippocampal neuronal cultures were prepared with embryos collected from E18-19 timed pregnant Sprague Dawley rats bred at Taconic Biosciences and housed at the NIH for 4-5 days prior to euthanasia.

Primary culture of rodent hippocampal neurons

Neuronal hippocampal cultures prepared from embryonic day 18-19 (E18) rodent embryos were performed as reported previously (69). Female dams were euthanized using CO_2 asphyxiation followed by guillotine decapitation. Embryos were rapidly dissected from the uterine horn, decapitated with sharp scissors, and whole heads were placed in ice-cold dissection medium (ThermoFisher, 1X HBSS (14185052), 1 mM sodium pyruvate (11360070), 10 mM HEPES (15630080), and 30 mM Glucose). After peeling away overlying skin and bone with forceps, brains were removed from the skull and placed into fresh dissection medium. Each hemisphere of the cerebral cortex was bisected from the hindbrain and the hippocampus was then gently rolled away and excised from the cerebral cortex and placed into fresh ice-cold dissection medium. Once all tissue was collected, the dissection medium was replaced with 5 ml room temperature (RT) papain solution (5 ml dissection solution w/ 1% DNase (Worthington, LK003170) and 1 vial 0.22 μm filtered Papain (Worthington, LK003176). After a 45 min RT incubation, tissue was washed 4x with prewarmed NB5 medium (5% FBS (Hyclone, SH30071.03), ThermoFisher: 1X Neurobasal A (21103049), 2% Glutamax (35050061), and 2% B27 (17504044). Tissue was dissociated by gentle trituration using a 5 ml plastic serological pipette, cells were filtered through a 70 μm cell strainer (Corning, 352350) and pelleted at 1,000 rpm in a swinging bucket centrifuge

(Beckman Coulter Allegra™ 6R) for 5 min at RT. Cells were resuspended in 10 ml NB5, diluted 1:1 in 0.4% Trypan Blue Stain (ThermoFisher, 15250061) and counted with a hemocytometer. Neurons were plated 125,000 (rat) or 175,000 (mouse)/well in a 12–well plate (Corning) containing glass coverslips. 12 mm round Poly-D-lysine/laminin pre-coated glass coverslips (Corning, 354087) were used for electrophysiology. For immunostaining and fluorescence microscopy neurons were plated on in-house Poly-D-lysine/laminin coated 18 mm German glass coverslips (Carolina Biological, 633013). Briefly, UV-sterilized coverslips were incubated overnight in poly-D-lysine (Sigma, P7280-5MG) dissolved in 22 µm filter-sterilized borate buffer (50 mM boric acid, 12.5 mM sodium borate, pH 8.5). The following day, coverslips were washed using sterile water and coated with 0.01 mg/ml mouse Laminin (ThermoFisher, 23017015) in PBS for 3 hrs. 24 hrs after seeding, NB5 was replaced with Neurobasal A (Invitrogen) supplemented as above but without FBS and 1% Glutamax (NB0). Neurons were fed twice per week thereafter by replacing 0.4 ml with 0.5 ml fresh NB0 per well.

Hippocampus area CA1 double immunogold electron microscopy

Animals used for postembedding, double-immunogold localization were prepared as described previously (117). Briefly, two male, adult Sprague Dawley rats were perfused with phosphate buffer, followed by perfusion with 4% paraformaldehyde + 0.5% glutaraldehyde in phosphate buffer, and then the brains were vibratomed, cryoprotected in glycerol overnight, frozen in a Leica EM CPC (Vienna, Austria), and embedded in Lowicryl HM-20 resin in a Leica AFS freeze-substitution instrument. Thin sections were incubated in 0.1% sodium borohydride + 50 mM glycine in Tris-buffered saline plus 0.1% Triton X-100 (TBST), then in 10% normal goat serum (NGS) in TBST, and then with 2 primary antibodies together in 1% NGS/TBST (overnight); then they were incubated with the 2 immunogold-conjugated secondary antibodies (5+15 nm; Ted Pella, Redding, CA, USA) in 1% NGS in TBST with 0.5% polyethylene glycol (20,000 MW), and stained with uranyl acetate and lead citrate. Controls on sections from the same two rats, labeled with the 2 secondary antibodies but without the primary antibodies, showed only rare gold and no colocalization.

Native hippocampal co-immunoprecipitation assays

We performed native co-IP experiments to confirm an interaction between endogenous Cav2.3 and Kv4.2 channel with male, 12-week-old wild type C57BL/6 or control Cav2.3-KO mouse hippocampus. Brain hippocampal tissue were lysed in lysis buffer: 150 mM NaCl, 20 mM Tris-HCl, 1% CHAPS and protease inhibitor mixture (Roche, USA) and incubated for 20 min on ice,

577 then sonicated 5 times for 5 s each. The lysate was centrifuged at 15,000 xg for 20 min at 4°C
578 and supernatants were incubated with anti-Cav2.3 (2 µg/500 µg protein) and guinea-pig IgG
579 (ThermoFisher Scientific) as nonspecific control. The mixture was then incubated and rotated at
580 4°C overnight. The antibody-antigen complex was adsorbed onto 50 µl of immobilized protein A
581 (ThermoFisher Scientific) and incubated and rotated for 2-3 h at 4 °C. The protein-bead mixtures
582 were washed 5x with lysis buffer. The beads were resuspended in SDS sample buffer
583 (ThermoFisher, NP0007) to elute bound proteins. Protein complexes were immunoblotted as
584 described below.
585
586 **COS7 cell surface biotinylation**
587 Biotinylation assays were performed as previously described (81). COS7 cells are our preferred
588 cell line for surface biotinylation because of a higher surface to volume ratio and slower dividing
589 time relative to HEK293 cells. COS7 cells were transfected with Kv4.2 and Cav2.3-GFP
590 constructs using X-tremegene 9 transfection reagent (Sigma-Aldrich, 06365779001) for 24-36 h;
591 the cells were rinsed with ice-cold PBS, and surface protein was biotinylated with 1.5 mg/ml sulfo-
592 NHS-SS-biotin reagent (ThermoFisher) in PBS for 30 min on ice. Unbound biotin was quenched
593 with cold 50 mM glycine in PBS. Cells were lysed with ice-cold lysis buffer: 150 mM NaCl, 20 mM
594 Tris-HCl, 1% CHAPS and protease inhibitor mixture (Roche Diagnostics), sonicated and
595 centrifuged at 12,000 g for 10 min. Cell lysates were incubated overnight at 4°C with immobilized-
596 Streptavidin agarose beads (ThermoFisher), and unbound protein was removed from the beads
597 with 5 washes in lysis buffer. The bound proteins were eluted with SDS sample buffer
598 (ThermoFisher, NP0007). Surface expressed and total proteins were immunoblotted as
599 described below.
600
601 **Western blots**
602 Sample proteins were separated on 3-8% Tris-acetate gels (ThermoFisher, EA03752) using SDS
603 buffer (ThermoFisher, NP0002) and electrophoresis chambers (ThermoFisher, EI0001). Proteins
604 were transferred using electrophoretic chambers (Bio-Rad, 1703930) in a Tris based buffer
605 (ThermoFisher, NP0006) to PVDF membranes (Millipore, IPFL00010). Immunoblots were
606 blocked for 1 h at RT and probed using primary antibodies overnight at 4°C in Odyssey blocking
607 buffer (Li-Cor Biosciences). After washes, immunoblots were probed for 1 h at RT with secondary
608 antibodies conjugated to infrared dyes for detection using the Odyssey infrared imaging system
609 (LI-COR Biosciences, Lincoln, NE). Quantification of results was performed using Odyssey
610 software.

Immunostaining

Brain slices: Deeply anesthetized mice were transcardially perfused with ice-cold paraformaldehyde (PFA) solution (4% PFA (Electron Microscopy Sciences, 15714-S), PBS, pH 7.4). Whole brains were dissected, post-fixed in 4% PFA for 4 h, and cryopreserved with increasing concentrations of sucrose solutions (10, 20 and 30% for 4, 12, and 12-24 h respectively). Cryopreserved brains were sectioned in a cryostat at 7 µm thickness (Histoserv, Inc.) through the dorsal hippocampus beginning at -1.955 mm caudal to bregma and adhered to microscope slides (Superfrost™ Plus, ThermoFisher, 1255015) and stored at -80°C. After thawing at RT for 15 min, a circle was drawn with a pap pen around each section to create a hydrophobic barrier. Sections were rehydrated using PBS for 5 min at RT and blocked for 1 h at RT (0.3% Triton X-100, 1% normal goat serum, PBS, pH 7.3-7.4). Next, fresh blocking solution containing primary antibodies was applied and incubated 24-48 h at 4°C in a closed, humidified box. Slides were washed 4 x 15 min in PBS with agitation. Secondary antibody was applied in 0.2% Triton X-100 PBS and sections were incubated while protected from light for 2 h at RT. Sections were washed 4 x 15 min in PBS with agitation. Coverslips were mounted using a DAPI-containing mounting medium (ProLong™ Gold Antifade, ThermoFisher, P36931).

Cultured hippocampal neurons: Primary neurons grown on glass coverslips were washed 1x with PBS and fixed in PFA solution for 10 min at RT. Neurons were washed 3 x 5 min with PBS and permeabilized using 0.2% Triton X-100 for 10 min at RT. After 3 x 1 min PBS washes, neurons were blocked with 3% BSA dissolved in PBS overnight at 4°C and protected from light. Primary antibodies were applied in 3% BSA PBS for 2 h at RT with gentle agitation. Neurons were washed 3 x 1 min in PBS and secondary antibodies dissolved in PBS were incubated for 1 h at RT with gentle agitation and protected from light. After 3 x 1 min washes, coverslips were mounted face-down on glass slides in mounting medium with DAPI (ProLong™ Gold Antifade, ThermoFisher, P36931).

Confocal fluorescence microscopy and analysis

PFA-fixed neuronal cultures and mouse brain slices were imaged using a Zeiss 710 laser scanning confocal microscope running Zen Black software (Zeiss Microscopy). Fluorescence was acquired using 405/449 nm (DAPI), 488/515 nm (Alexa 488), and 633/670 (Alexa 647) nm laser excitation/emission wavelengths. Hippocampal sections were imaged using a Zeiss 10x Plan-Apochromat 10x/0.45NA air objective capturing 0.83 µm/pixel in *x* and *y* dimensions. Z-stacks were 20.83 µm tall with a 5.21 µm step size. A Zeiss 63x Plan-Apochromat/1.4NA oil objective

644 was used for cultured neurons yielding 0.13 μm/pixel in *x* and *y* dimensions. Z-stacks were 3.36
645 μm tall using 0.42 μm z-steps, and max intensity projections were used for analysis. Analysis was
646 performed in ImageJ (NIH). Spine and dendrite fluorescence intensities were measured by
647 masking all clearly identifiable mushroom-shaped spines and adjacent dendrite segments from
648 which they projected. Spine/dendrite ratios were calculated from the mean spine and dendrite
649 shaft intensities from each cell.
650
651 **Live-cell FRET microscopy in HEK293FT cells**
652 *FRET Acquisition:* Cultured HEK293FT cells were trypsinized ≤ 2 min, counted, and 75,000 cells
653 were seeded onto uncoated 18 mm glass coverslips. After 24 h growth, cells were transfected
654 using OPTI-MEM serum free medium, X-tremeGene 9 (Sigma, 6365779001) and various
655 plasmids. Living cells were imaged in a Tyrode's salt solution (in mM: 135 NaCl, 5 KCl, 2 $CaCl_2$,
656 1 $MgCl_2$, 25 HEPES, 10 glucose, pH 7.4) at RT 24–48 h post-transfection. An Observer.Z1
657 microscope (Zeiss) with a 63x plan-apochromat, 1.4 NA oil objective (Zeiss), Lambda LS Xenon
658 Arc Lamp Light Source System (Sutter Instruments), AxioCam MRm camera (Zeiss), and Zen
659 Blue software (Zeiss) were used for image acquisition. Three-filter FRET images were captured
660 using appropriate filter cubes (Semrock) housed in the microscope turret. CFP cube: (Ex. 438/24
661 nm, Em. 483/32 nm, Di. 458 nm), YFP cube: (Ex. 500/24 nm, Em. 542/27 nm, Di. 520 nm), and
662 FRET cube: (Ex. 438/24 nm, Em. 542/27 nm, Di. 458 nm). ImageJ software (NIH) was used for
663 image processing and calculations of sensitized FRET efficiency were adapted from the method
664 of Clemens Kaminski (118) with more details provided below.

665 *FRET analysis:* CFP, YFP, and CFP-YFP rawFRET fluorescence were captured in
666 single *xy* planes using the following excitation and detection scheme:

667 CFP image: CFP excitation and CFP emission (CFP fluorescence intensity)

668 YFP image: YFP excitation and YFP emission (YFP fluorescence intensity)

669 rawFRET image: CFP excitation and YFP emission (uncorrected FRET fluorescence intensity)

670 Fluorescence background was estimated by measuring the mean pixel values for several images
671 captured in a cell-free section of the coverslip on the experimental day. After background
672 subtraction, fluorescence intensity in the rawFRET image was corrected for CFP bleed-through
673 and YFP cross-excitation. A significant percentage of the fluorescent signal in the rawFRET image

674 is not due to FRET, but instead results from spectral crosstalk that must be subtracted. A
675 percentage of fluorescence emission from CFP is present in the YFP emission bandpass of the
676 rawFRET image (CFP bleed-through). Conversely, YFP cross-excitation occurs when CFP
677 excitation bandpass in the rawFRET image leads to direct excitation of YFP. For each FRET pair,
678 CFP bleed-through and YFP cross-excitation in the rawFRET image was measured by expressing
679 either the CFP or YFP construct alone and determining the ratio of fluorescence intensity in the
680 rawFRET image divided by the fluorescence intensity in the CFP (donor emission ratio (DER) or
681 YFP (Acceptor emission ratio (AER)) image across many cells. Each FRET pair yields unique
682 spectral cross-talk that when subtracted from the rawFRET image, generates the true signal due
683 to CFP/YFP FRET, known here as corrected FRET (FRETc). The equation

684 $$FRETc = rawFRET - (DER \times CFP) - (AER \times YFP)$$

685 was used to determine the amount of FRET in each cell. Mean CFP, YFP, and raw FRET
686 fluorescence intensities were measured by mask analysis of regions enriched for the construct of
687 interest. For cells expressing 1:1 stoichiometry of CFP and YFP, apparent FRET efficiency values
688 were calculated from mean intensities and normalized to the fraction of acceptor molecules
689 undergoing FRET ($FRET\ EFF_A$) using the equation:

690 $$FRET\ EFF_A = \frac{FRETc}{AER \times YFP \times \beta}$$

691 where β is a factor relating spectral and excitation efficiencies of donor and acceptor molecules.
692 For experiments measuring the stoichiometry of CFP/YFP FRET pairs, cells were transfected with
693 various ratios of CFP and YFP cDNAs and imaged as above. In addition to measuring FRET
694 EFF_A, FRET EFF_D was calculated using the equation:

695 $$FRET\ EFF_D = \frac{FRETc\ \frac{\alpha}{DER}}{CFP + FRETc\frac{\alpha}{DER}}$$

696 where α relates the quantum yields and signal detection efficiencies between donor and
697 acceptors. The values for α and β were found using the method of Kaminski (118). Briefly, using
698 the wide-field microscopy system described above, transfection of a control CFP-YFP tandem
699 fusion construct consisting of CFP and YFP separated by an 18 amino acid linker

(GLRSRAQASNSAVEGSAM) with a predetermined FRET efficiency of 0.38 allows for determination of α and β using the following equations:

$$\alpha = \frac{0.38}{1 - 0.38} \frac{DER \times CFP}{FRETc}$$

$$\beta = \frac{FRETc}{AER \times YFP \times 0.38}$$

Plotting either FRET EFF_A vs. CFP/YFP or FRET EFF_D vs. YFP/CFP gives a measure of saturating FRET at either the acceptor or donor. The ratio of the maximum FRET value normalized for acceptor or donor concentration approximates the stoichiometry of the interaction as described by others (66, 119, 120).

Fluorescence recovery after photobleaching (FRAP) microscopy

FRAP acquisition: Fluorescence imaging was performed on a Zeiss 710 laser scanning confocal microscope equipped with a 405-30 nm diode laser, tunable Argon laser, DPSS 561-10 nm laser, and a Zeiss 63x Plan-Apochromat/1.4 NA oil objective. A stage insert incubation system was used to maintain cells at 34°C. Samples were illuminated at low laser power (2.0-3.5%). Image acquisition and ROI bleaching was driven by Zen Black software (Zeiss Microscopy). Images were acquired at 4X zoom yielding 0.033 μm/pixel. Cells were imaged 24-48 hrs after transfection in Tyrode's salt solution. For HEK293FT cells, 500,000 cells were seeded onto 25 mm coverslips in 6-well cell culture dishes (Corning). After 24 h, cells were transfected with CFP, YFP, Kv4.2-CFP, or YFP-Cav2.3 constructs using X-tremeGene 9 Transfection Reagent (Sigma-Aldrich, 06365779001). Samples were illuminated at low laser power with either 405 nm or 515 nm laser excitation, PMT gain of 700, and at 0.5 Hz. Both CFP and YFP fluorescence were photobleached within a 50 px^2 ROI using 8 iterations of the 405 nm laser at 100% power. For cultured neurons, DIV12-13 neurons were transfected with Kv4.2-sGFP2 and mCherry using Lipofectamine 2000 Transfection Reagent (ThermoFisher, 52887). Samples were illuminated with 488 nm and 560 nm laser excitation, PMT gain of 700-750, and at 0.2 Hz. Kv4.2-SGFP2 fluorescence was photobleached within a 30 px^2 ROI for dendrite shafts and a custom ROI matching the shape of each spine. Both dendrite and spine photobleaching required 8 iterations of the 405 nm laser at 100% power.

FRAP data analysis: FRAP data was processed and analyzed as previously described (121) using the double normalization method described by Phair and Misteli (122),

$$I_{norm} = \frac{ref_{pre} \times (I_{FRAP}(t) - I_{bkgd}(t))}{(I_{ref}(t) - I_{bkgd}(t)) \times frp_{pre}}$$

Where ref_{pre} and frp_{pre} are the background corrected means of the pre-bleach time points from the reference and FRAP region intensity traces, respectively. $I_{FRAP}(t)$ is the fluorescence intensity within the FRAP ROI, $I_{bkgd}(t)$ is a background intensity from an ROI outside the cell, and $I_{ref}(t)$ is the reference intensity in an unbleached region of the cell to account for photobleaching during acquisition. FRAP curves from individual ROIs were vetted for adequate bleaching (≥ 50% post-bleach intensity compared to pre-bleach intensity) and stability of intensity trace (e.g., traces with distortions due to cellular movement or stage-drift were discarded). After screening, normalized curves were then scaled 0 to 1 and averaged. Standard deviation and standard error of the mean were calculated. Averaged curves were fitted with a single-exponential, $FRAP(t) = A \times (1 - e^{-\tau \times t})$, where A is the mobile fraction using GraphPad Prism software.

HEK293FT cell whole-cell voltage-clamp recordings

HEK293FT cells were seeded onto 35 mm cell culture dishes at a concentration of 500 x 10^6 cells per dish. After 16-24 h, cultures were transfected with various plasmids (1-2 μg). To each dish, DNA was first mixed with 300 μl Opti-MEM Reduced Serum Medium (ThermoFisher, 31985070) reduced serum medium. Next, 6 μl X-tremegene 9 DNA Transfection Reagent (Sigma-Aldrich, 06365779001) was added and incubated for 10 min at room temperature before dropwise addition to cultures. On the day of recording (24-48 h after transfection), cultures were trypsinized for ≤ 2 min and seeded at low density onto glass coverslips and allowed to adhere ≥ 1 h. Coverslips were then transferred to a recording chamber and superfused (1-2 ml min^{-1}) in 95% O_2, 5% CO_2 saturated extracellular solution (in mM: 115 NaCl, 2.5 KCl,1.25 NaH_2PO_4, 25 $NaHCO_3$, 2 $CaCl_2$, 1 $MgCl_2$, 25 glucose, pH 7.2-7.3; 300 mOsm/l) at RT. Borosilicate patch electrodes were pulled using a two-stage pipette puller (Narishige PC-10) to a tip resistance of 2.5-4.0 MΩ. Patch electrodes were filled with (in mM): 115 KCl, 10 NaCl, 20 KOH, 10 Hepes, 10 EGTA, and 25 glucose (pH 7.3, 290 mOsm). Maximum voltage-gated K^+ currents were elicited by voltage steps from a holding potential (-70 mV) to -120mV for 400 ms to relieve Kv4.2 channel inactivation and to +60 mV for 400 ms to maximize channel opening. Inactivation rates were measured by fitting the falling phase of macroscopic currents with a double exponential decay. Voltage dependence of activation was performed using the same holding and hyperpolarizing steps as above but with

a range of intermediate activation potentials (-100, -80, -60, -40, -30, -20, -10, 0, +10, +20, +30, +40, and +60 mV). Voltage-dependence of inactivation was determined using 400 ms conditioning steps from holding to -140, -130, -120, -100, -80, -60, -40, -20, -10, and 0 mV immediately before a 400 ms step to +60 mV. Recovery from inactivation was measured using two 400 ms voltage steps to +60mV separated by various intervals (5, 10, 15, 20, 25, 50, 100, 200, and 500 ms).

Cultured neuron whole-cell voltage-clamp recordings

Primary hippocampal cultured neurons were grown on 12 mm coverslips to DIV6-9 for whole cell recordings or DIV21-27 for miniature excitatory postsynaptic current recordings. At the time of recording, a coverslip was transferred from a 12-well culture plate to the recording chamber and superfused in extracellular solution as described above for HEK293FT cells. Patch electrodes were pulled as described above to a tip resistance of 5-7 MΩ and back-filled with an internal solution containing (in mM): 20 KCl, 125 K-gluconate, 5 EGTA, 4 NaCl, 4 Mg^{2+}-ATP, 0.3 Na-GTP, 10 HEPES, and 10 phosphocreatine (pH 7.2, 290 mOsm). Once whole-cell configuration was achieved, neurons were held at -60 mV between voltage protocols. I_A was evoked with a 400 ms conditioning step to -80 mV to relieve inactivation before stepping to 0 mV for 400 ms. I_A was recorded in the presence of bath applied drugs to block contaminating postsynaptic currents: (in μM) 0.5 Tetrodotoxin (TTX) (Tocris, 1069), 1.0 SR 95531 hydrobromide (Gabazine) (Tocris, 1262), 10.0 CNQX-Na^2 (Tocris, 1045), and 2.0 MK-801 maleate (Tocris, 0924). The voltage protocol was repeated every 5 seconds for 6 min. Drugs were applied by rapid perfusion (3 ml/min) 20 sec after recordings began. IC_{50} for Ni^{2+} block of I_A was determined using a single exponential fit to the dose-response curve. For measurements of the voltage-dependence of inactivation, 400 ms conditioning steps from holding to -120, -100, -80, -70, -60, -50, -40, -20, -10, and 0 mV immediately before a 400 ms step to 0 mV. Inactivation curves were fit to a Boltzmann function. Miniature excitatory postsynaptic currents (mEPSCs) were recorded in the presence of TTX and Gabazine. For mEPSC recordings in the presence of bath applied Ni^{2+} or AmmTX3, a 10 min wash-in period ensured efficient R-current and I_A block, respectively before patching. Immediately after break-in, mEPSCs were recorded in 2 min epochs at a holding potential of -70 mV. Event amplitude was measured by the “Threshold Search” event detection procedure in Clampfit. A maximum of 200 events from each neuron were included for analysis.

Hippocampal slice preparation and CA1 pyramidal neuron recordings

6-8 week-old male mice were anesthetized with isoflurane and decapitated. For cell-attached dendritic recordings, mice were trans-cardially perfused with ice-cold slicing solution before

796 decapitation. Brains were then transferred into ice-cold slicing solution containing in mM: 2.5 KCl,
797 28 $NaHCO_3$, 1.25 NaH_2PO_4, 7 Glucose, 0.5 $CaCl_2$, 7 $MgCl_2$, 233 Sucrose, and bubbled with 95%
798 O2 / 5% CO2. Transverse slices of the hippocampus (300 µm) were made using a Leica VT1200S
799 vibrating microtome. Slices were transferred to 32ºC ACSF containing in mM: 125 NaCl, 2.5 KCl,
800 25 $NaHCO_3$, 1.25 NaH_2PO_4, 25 Glucose, $2CaCl_2$, 1 $MgCl_2$, 1 ascorbic acid, 3 Na-Pyruvate, and
801 bubbled with 95% O2 / 5% CO2. After 25 minutes the slice chamber was transferred to room
802 temperature for the rest of the recording day. For recording, slices were transferred to a recording-
803 chamber with continuous flow of ACSF (2-3ml/min). Recording pipettes for somatic whole cell and
804 outside-out patch recordings had a tip-resistance of 3-5 MΩ and were filled with an internal
805 solution containing in mM: 20 KCl, 125 K-Gluconate, 1 EGTA, NaCl, 4 NaCl, Mg-ATP, 0.3 NaGTP,
806 10 HEPES, 10 Phosphocreatine, pH 7.26, 296 mOsm. Recording pipettes for dendritic cell-
807 attached voltage-clamp were filled with an internal solution mimicking ACSF, containing in mM: 3
808 KCl, 125 NaCl, 10 HEPES, 25 Glucose, $2CaCl_2$, 1 $MgCl_2$, pH 7.24, 290 mOsm. Dendritic cell-
809 attached recordings were performed in voltage-clamp mode and voltage step protocols have been
810 inverted for readability in the results section, to account for the reversed polarity of the cell-
811 attached recordings. Protocols were designed for a theoretical resting membrane potential of -
812 60mV. I_A was calculated by subtracting I_{sus} from I_{tot}. I_{tot} was elicited using a voltage step to +40
813 from a -120 mV pre-pulse and a subsequent step to +40 from -30 mV was used to isolate I_{sus}.
814 Bath ACSF was supplemented with 1µM TTX to block voltage-gated sodium channels, 1µM
815 Gabazine to selectively block GABAA receptors, and 10µM CNQX to block AMPA-type and
816 Kainate-type glutamate receptors. Recording electrodes were pulled to 10-12 MΩ using a
817 Narishige PC-10 pipette puller and polished using a Narishige microforge.
818
819 **Electrophysiology equipment, data processing, and analysis**
820 Manual patch clamp experiments were performed on an Axioskop 2 FS Plus microscope (Zeiss)
821 with CP-Achromat 10× 0.25 air (Zeiss) and LumplanFL 60× 1.0 NA water immersion (Olympus)
822 objectives, and Sutter MPC-200 multi manipulator system with ROE-200 controller. The rig was
823 equipped with a Sutter LB-LS/17 lamp for fluorescence and DIC optics. An Axon Multiclamp 700B
824 amplifier, Axon Digidata 1440A A/D converter,and PClamp software (Molecular, Devices,
825 Sunnyvale, CA) were used to acquire electrophysiological signals. Currents were normalized to
826 cell size using whole-cell capacitance upon cell break-in, and leak currents were subtracted using
827 a P/4 protocol. Data were analyzed using Microsoft Excel, MATLAB, IGOR Pro (WaveMetrics,
828 Lake Oswego, OR), and GraphPad Prism. Pooled data are presented as either bar graphs ± SEM
829 overlaid with individual data points or in tabular format ± SEM.

Cultured hippocampal neuron Ca^{2+} imaging and analysis

Fast confocal imaging was performed using a 25× 1.1 NA water immersion objective on an A1R MP HD system (Nikon) coupled to a Retiga ELECTRO CCD camera (QImaging) used for sample scanning. Time-series were captured at 15.3 Hz using a 6x zoom on a resonant scanner yielding 0.08 μm/pixel. Image acquisition was controlled by Elements software (Nikon) and analysis was performed in ImageJ (NIH). DIV13-15 primary hippocampal neurons grown on 18 mm glass coverslips were transfected 24-48 h before imaging using Lipofectamine 2000. Neurons were transfected with the genetically encoded Ca^{2+} indicator GCaMP6f and mCherry as a marker of neuronal morphology. Coverslips were transferred to a quick release magnetic imaging chamber (Warner, QR-41LP) with constant perfusion (1-2 ml/min) of modified Tyrode's salt solution (3 mM $CaCl_2$, 0 mM $MgCl_2$, 10 μM glycine, 0.5 μM TTX) at RT. Spine Ca^{2+} signals were analyzed by drawing a mask over the spine of interest. Mean GCaMP6f fluorescence intensity was measured using the "Plot Z-axis Profile" function in imageJ. Extracted intensity values were background subtracted and normalized to baseline fluorescence intensity ($\Delta F/F_0$). Only a transient $>$ 2.5 fold above baseline was used for analysis. Many of the analyzed Ca^{2+} transients were clearly individual events; however, if two or more transients overlapped, we developed rules to discern whether they should be considered multiple events. For a trailing event to be considered a unique event, the first transient must have dropped $>$50% of maximum. Additionally, the trailing transient must rise $>$50% above the lowest $\Delta F/F_0$ of the previous spike to be considered a separate event. If a trailing transient did not meet both criteria it was not considered unique from the initiating transient.

ACKNOWLEDGEMENTS

This work was supported by the Intramural Research Program of the Eunice Kennedy Shriver National Institute of Child Health and Human Development (J.G.M., J.J.G., L.L., J.H., and D.A.H.) and the National Institute of General Medical Sciences Postdoctoral Research Associate Training Grant (FI2 GM12004) (J.G.M.). Support was also provided by the Intramural Research Program of NIH/National Institute on Deafness and Other Communication Disorders (NIDCD) (Advanced Imaging Core-ZIC DC000081) (R.S.P. and Y-X.W.). We thank members of the Hoffman Lab for valuable discussions, protocols, and experimental assistance. We would like to thank Mark Dell'Acqua and for comments on this manuscript. We are grateful to Adriano Bellotti for contributing cultured rat neurons used in some experiments. The Ca^{2+}-dead KChIP2c construct was generated by site directed mutagenesis by Jung Park. Ying Liu bred, genotyped, and cared for the WT and Cav2.3 KO mice used in this work. We thank Vincent Schram (NICHD Microscopy & Imaging Core) for technical assistance.

COMPETING INTERESTS

Pertinent to contents of this manuscript, the authors have no competing financial or institutional interests to declare.

A

Protein	Number of peptides (Unique)	Number of peptides (Total)	% of aa sequence coverage
Kv4.2	96	386	67.30%
Kv4.1	21	35	31.07%
Kv4.3	25	33	37.56%
DPP6	7	8	9.78%
DPP10	2	2	2.14%
KChIP1	8	20	30.84%
KChIP2	7	8	27.04%
KChIP3	4	9	25.00%
KChIP4	8	16	33.20%

B

Cav2.3 sequence:

```
1 malynpipvr qncftvnrsl fifgednivr kyakklidwp pfeymilati iancivlale 61
qhlpeddktp msrrlektep yfigifcfea gikivalgfi fhkgsylrng wnvmdfivvl 121
sgilatagth fnthvdlrtl ravrvlrplk lvsgipslqi vlksimkamv pllqiglllf 181
failmfaiig lefysgklhr acfmnnsgil egfdpphpcg vqgcpagyec kdwigpndgi 241
tqfdnilfav ltvfqcitme gwttvlyntn dalgatwnwl yfipliiigs ffvlnlvlgv 301
lsgefakere rvenrrafmk lrrqqqiere lngyrawidk aeevmlaeen knsgtsalev 361
lrratikrsr teamtrdssd ehcvdissvg tplarasiks tkvdgasyfr hkerllrisi 421
rhmvksqvfy wivlsvvaln tacvaivhhn qpqwlthlly yaeflflglf llemslkmyg 481
mgprlyfhss fncfdfgvtv gsifevvwai frpgtsfgis vlralrllri fkitkywasl 541
rnlvvslmss mksiisllfl lflfivvfal lgmqlfggrf nfndgtpsan fdtfpaaimt 601
vfqiltgedw nevmyngirs qggvssgmws aiyfivltlf gnytllnvfl aiavdnlana 661
qeltkdeqee eeafnqkhal qkakevspms apnmpsierd rrrrhhmsmw eprsshlrer 721
rrrhhmsvwe qrtsqlrrhm qmssqealnk eeappmnpln plnplsplnp lnahpslyrr 781
prpieglalg lglekceeer isrggslkgd iggltsvldn qrsplslgkr eppwlprsch 841
gncdptqqet gggetvvtfe drarhrqsqr rsrhrrvrte gkesasasrs rsasqersld 901
egvsidgeke hepqsshrsk eptiheeert qdlrrtnslm vprgsglvga ldeaetplvq 961
pqpelevgkd aalteqeaeg sseqalladv qldvgrgisq sepdlscmtt nmdkattest 1021
svtvaipdvd plvdstvvni snktdgeasp lkeaetkeee eevekkkqkk ekretgkamv 1081
phssmfifst tnpirkachy ivnlryfemc illviaassi alaaedpvlt nsernkvlry 1141
fdyvftgvft femvikmidq glilqdgsyf rdlwnildfv vvvgalvafa lanalgtnkg 1201
rdiktikslr vlrvlrplkt ikrlpklkav fdcvvtslkn vfnlivykl fmfifaviav 1261
qlfkgkffyc tdsskdteke cignyvdhek nkmevkgrew krhefhydni iwalltlftv 1321
stgegwpqvl qhsvdvteed rgpsrsnrme msifyvvyfv vfpfffvnif valiiitfqe 1381
qgdkmneecs lekneracid faisakpltr ympqnrhtfq yrvwhfvvsp sfeytimami 1441
alntvvlmmk yysapwtyel alkylniaft mvfslecvlk viafgflnyf rdtwnifdfi 1501
tvigsiteii ltdsklvnts gfnmsflklf raarlikllr qgytirillw tfvqsfkalp 1561
yvclliamlf fiyaiigmqv fgnikldees hinrhnnfrs ffgslmllfr satgeawqei 1621
mlsclgekgc epdttapsgq neserctdl ayvyfvsfif fcsflmlnlf vavimdnfey 1681
ltrdssilgp hhldefvrvw aeydraacgr ihytemyeml tlmspplglg krcpskvayk 1741
rlvlmnmpva edmtvhftst lmalirtald ikiakggadr qqldselqke tlaiwphlsq 1801
kmldllvpmp kasdltvgki yaammimdyy kqskvkkqrq qleeqknapm fqrmepsslp 1861
qeiisnakal pylqqdpvsq lsgrsgypsm splspqeifq lacmdpaddg qfqeqqslvv 1921
tdpssmrrsf stirdkrsns swleefsmer ssentyksrr rsyhsslrls ahrlnsdsgh 1981
ksdthrsggr ergrskerkh llspdvsrcn seergtqadw esperrqsrs psegrsqtpn 2041
rqgtgslses sipsisdtst prrsrrqlpp vppkprplls ysslmrhtgg ispppdgseg 2101
gsplasqale snsacltess nslhpqqggh pspqhyisep ylalhedsha sdcgeeetlt 2161
feaavatslg rsntigsapp lrhswqmpng hyrrrrlggl glammcgavs dllsdteedd 2221 kc
```

C

Position	Peptide	Δcorr	Xcorr
19-30	SLFIFGEDNIVR	0.148	2.48
352-362	NSGTSALEVLR	0.174	2.03
403-410	VDGASYFR	0.141	1.94
809-822	GDIGGLTSVLDNQR	0.345	2.9
1516-1528	LVNTSGFNMSFLK	0.052	2.19
1869-1884	ALPYLQQDPVSGLSGR	0.504	4.22
1938-1950	SNSSWLEEFSMER	0.402	2.76

Figure 1 – Figure Supplement 1. A tandem affinity purification-mass spectrometry screen identifies Cav2.3 as a binding partner of Kv4.2.

A. The numbers of unique and total peptides, and the percent (%) amino acid sequence coverage for each protein that are presented in hippocampal neurons. **B.** Amino acid sequence coverage obtained for Cav2.3 protein from rat hippocampal neurons. Peptides detected by MS are underlined. **C.** Cav2.3 protein sequence report. Xcorr: Sequest cross-correlation score; Δcorr: Xcorr difference between the top ranked and next best sequence.

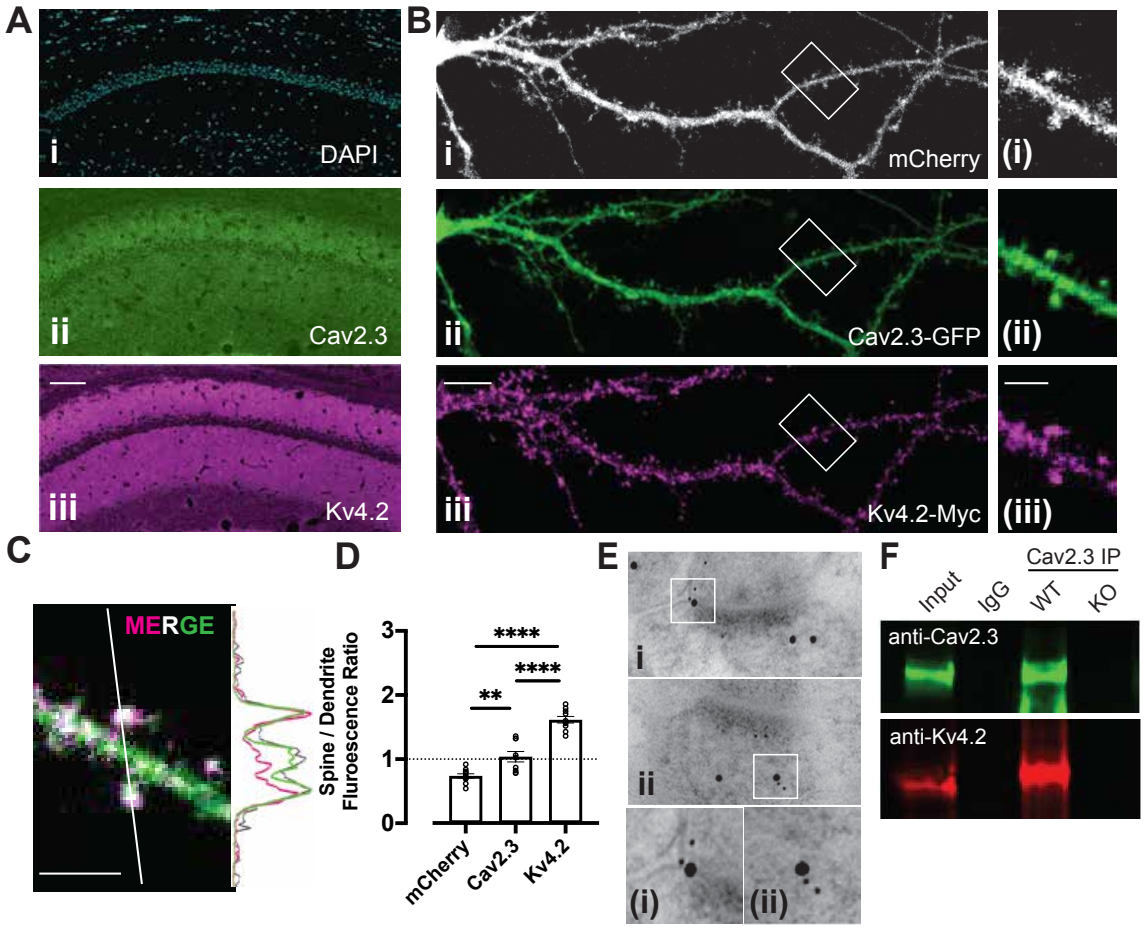

Figure 1. Cav2.3 and Kv4.2 colocalize in hippocampal neurons.

A. Mouse hippocampal brain sections were stained for (**Ai**) nuclei (DAPI), (**Aii**) Cav2.3, and (**Aii**) Kv4.2 channels. Cav2.3 and Kv4.2 are localized to dendrite fields of hippocampal area CA1. 100 μm scale bar **B.** Primary rat hippocampal neurons expressing (**Ai**, white) mCherry, (**Aii**, green) Cav2.3-GFP, and (**Aiii**, magenta) Kv4.2-myc. (Inset) Cav2.3 and Kv4.2 channel fluorescence is enriched in dendritic spines relative to mCherry. 10 μm and 3 μm scale bars **C.** Merged Kv4.2-myc and Cav2.3-GFP fluorescence of dendritic segment in panel **B**. The intensity profile demonstrates spine enrichment of both Cav2.3-GFP and Kv4.2-myc. 3 μm scale bar **D.** Cav2.3-GFP and Kv4.2-myc are enriched in spines when compared to cytosolic mCherry. n = 10; ** $p < 0.01$; **** $p < 0.0001$ by one-way ANOVA with Tukey's multiple comparison. **E.** Double immunogold electron micrographs of rat hippocampal sections labeled using 5 nm (Cav2.3) and 15 nm gold (Kv4.2). (insets) Cav2.3 and Kv4.2 colocalize within postsynaptic spines. **F.** Cav2.3 immunoprecipitation (green) pulls down Kv4.2 (red) from native hippocampal tissue.

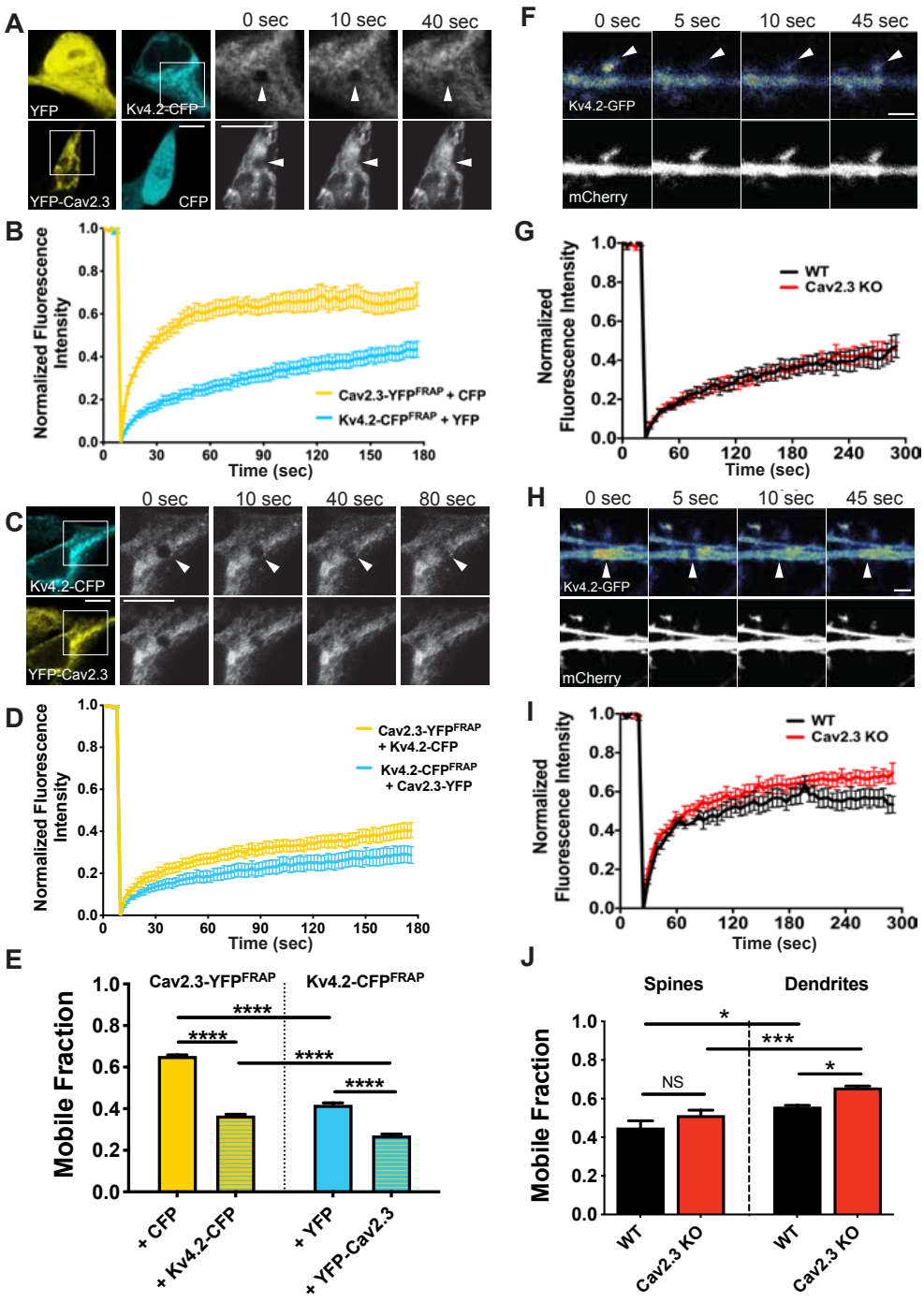

Figure 2. Cav2.3 regulates Kv4.2 mobility in HEK293FT cells and neuronal dendrites.

A. HEK293FT cells were transfected with either YFP and Kv4.2-CFP (above) or YFP-Cav2.3 and CFP (below). FRAP time series for Kv4.2-CFP (above) or YFP-Cav2.3 (below) in gray scale. 5 μm scale bars. **B.** Fluorescence recovery within the bleached volume is plotted over time for Kv4.2-CFP and YFP-Cav2.3 when expressed with non-interacting fluorescent proteins (YFP and CFP, respectively). **C.** Representative images of coexpressed Kv4.2-CFP (above) and YFP-

Cav2.3 (below) and coincident FRAP time series are shown in gray scale. 5 μm scale bars. **D.** FRAP recovery curves are plotted for coincident bleaching of Kv4.2-CFP and YFP-Cav2.3. **E.** Averaged FRAP curves were fit with a single exponential and mobile fraction was plotted in bar graphs for comparison among conditions. Coexpression of Kv4.2-CFP and YFP-Cav2.3 reduces respective mobile fractions consistent with reciprocal interactions between the two channels. (n = 15-19 cells for each condition across 3 experiments) **F.** Dendrite Kv4.2-SGFP2 FRAP in a WT mouse hippocampal neuron expressing Kv4.2-GFP (pseudocolor) and mCherry (white). 2 μm scale bar. **G.** Dendrite Kv4.2-SGFP2 FRAP is plotted over time in WT (black) and Cav2.3 KO mouse neurons (red). **H.** Spine Kv4.2-SGFP2 FRAP is shown as in F. 2 μm scale bar. **I.** Spine Kv4.2-SGFP2 FRAP is plotted as in G. **J.** Bar graphs show mobile fraction extracted from single exponential fits of averaged FRAP curves. Kv4.2-SGFP2 mobile fraction was significantly higher in dendrites compared to spines. A larger Kv4.2-SGFP2 mobile fraction was detected in dendrites of Cav2.3 KO mouse neurons when compared to WT. n = 17-18 spines and 14-17 dendrites from 7 WT and 7 Cav2.3 KO neurons. Data was pooled from 2-3 hippocampal cultures. Error bars represent +/- SEM. * $p < 0.05$, *** $p < 0.001$, **** $p < 0.0001$. Statistical significance was evaluated by one-way ANOVA with Tukey's multiple comparisons test.

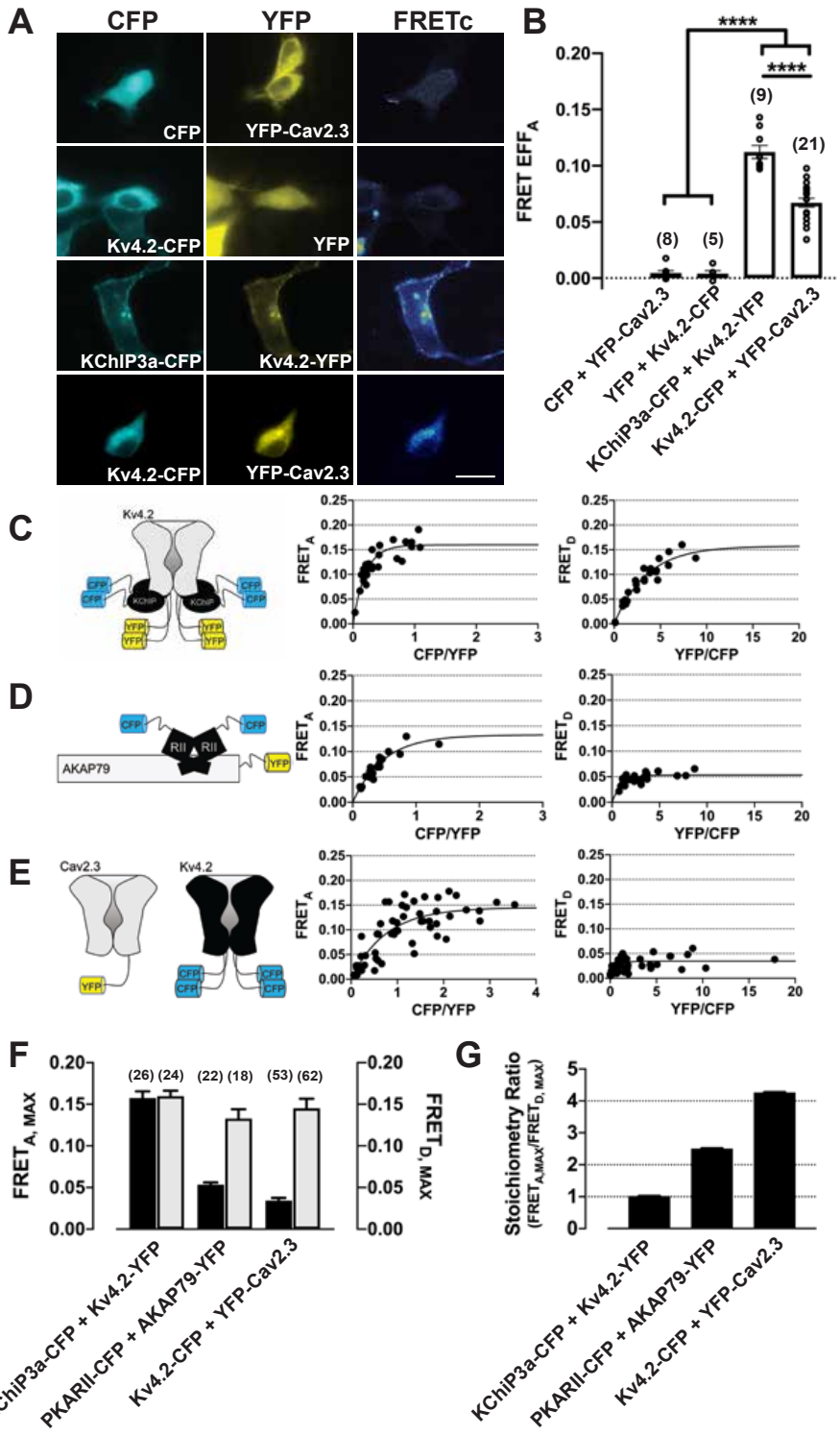

Figure 3. Cav2.3 and Kv4.2 bind at a 1:1 ion channel stoichiometry within a cellular nanodomain.

A. Representative raw CFP (cyan), YFP (yellow), and FRETc (pseudocolor) fluorescent images of HEK293FT cells expressing FRET constructs at equimolar concentrations. **B.** Bar graphs show

963 comparison of mean FRET efficiency normalized to acceptor concentration for each condition.
964 Parentheses indicate n values from 2-3 independent experiments. **C-E.** Left, cartoons depict the
965 expected stoichiometry of Kv4.2-YFP and KChIP2c-CFP (1:1) and AKAP79-YFP and PKARIIα-
966 CFP (1:2) while YFP-Cav2.3 and Kv4.2-CFP stoichiometry is inferred from the data. Right, cells
967 were transfected with various ratios of plasmid DNA. Donor and acceptor normalized FRET
968 efficiency were plotted for each cell over the ratio of donor and acceptor fluorescence. **F.** Bar
969 graphs compare acceptor (grey bars) and donor (black bars) normalized FRET efficiency for each
970 condition. Parentheses indicate n values from 2-3 biological replicates. **G.** FRET stoichiometry
971 ratio is calculated using the formula $FRET_{A,MAX}/\ FRET_{D,MAX}$ is plotted for FRET pairs confirming a
972 1:4 ratio of acceptor:donor or a 1:1 channel stoichiometry due to the tetrameric structure of Kv4.2.
973 Error bars represent +/- SEM. **** $p < 0.0001$. Statistical significance was evaluated by one-way
974 ANOVA with Tukey's multiple comparisons test.
975
976

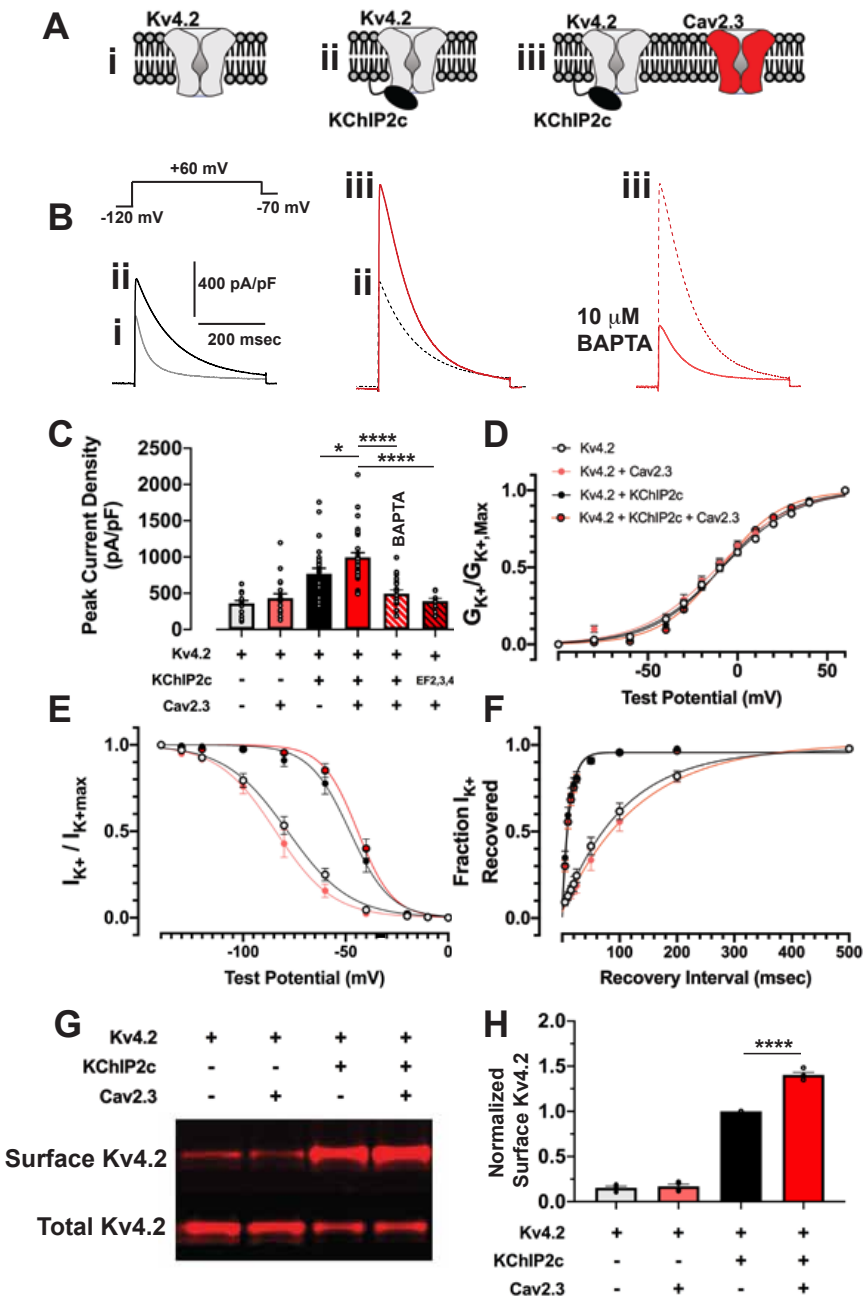

Figure 4. Cav2.3 expression increases Kv4.2 current density in a KChIP- and Ca^{2+}-dependent manner in HEK293FT cells.

A. Cartoons depict a subset of transfection conditions with either Kv4.2 alone (**i**), Kv4.2 and KChIP2c (**ii**), or Kv4.2, KChIP2c, and Cav2.3 (**iii**). **B.** Representative traces from conditions shown in A. **C.** Bar graphs plot peak Kv4.2 current density under the conditions shown, n = 10-32 cells. Cav2.3 expression increases Kv4.2 current density in a KChIP-dependent manner, which is reversed by replacement of EGTA with BAPTA in the patch pipette and by coexpression of EF-dead KChIP2c. **D.** Kv4.2 voltage-dependence of activation is plotted using normalized

conductance against a range of membrane test potentials and fit to a Boltzmann function. **E.** Kv4.2 voltage-dependance of inactivation is plotted using normalized current against conditioning test potentials and fit to a Boltzmann function. **F.** Kv4.2 recovery from inactivation is plotted as the fraction of current recovered using a +60 mV test potential from an initial test potential of the same magnitude against various recovery intervals. **G.** Representative western blot of a surface biotinylation assay in COS7 cells transfected according to the indicated conditions. **H.** Bar graph shows Kv4.2 surface expression normalized by day of experiment to the Kv4.2 and KChIP2c expression condition. Error bars represent +/- SEM from 4 biological replicates. *$p < 0.05$, **** $p < 0.0001$. Statistical significance was evaluated by one-way ANOVA with Tukey's multiple comparisons test.

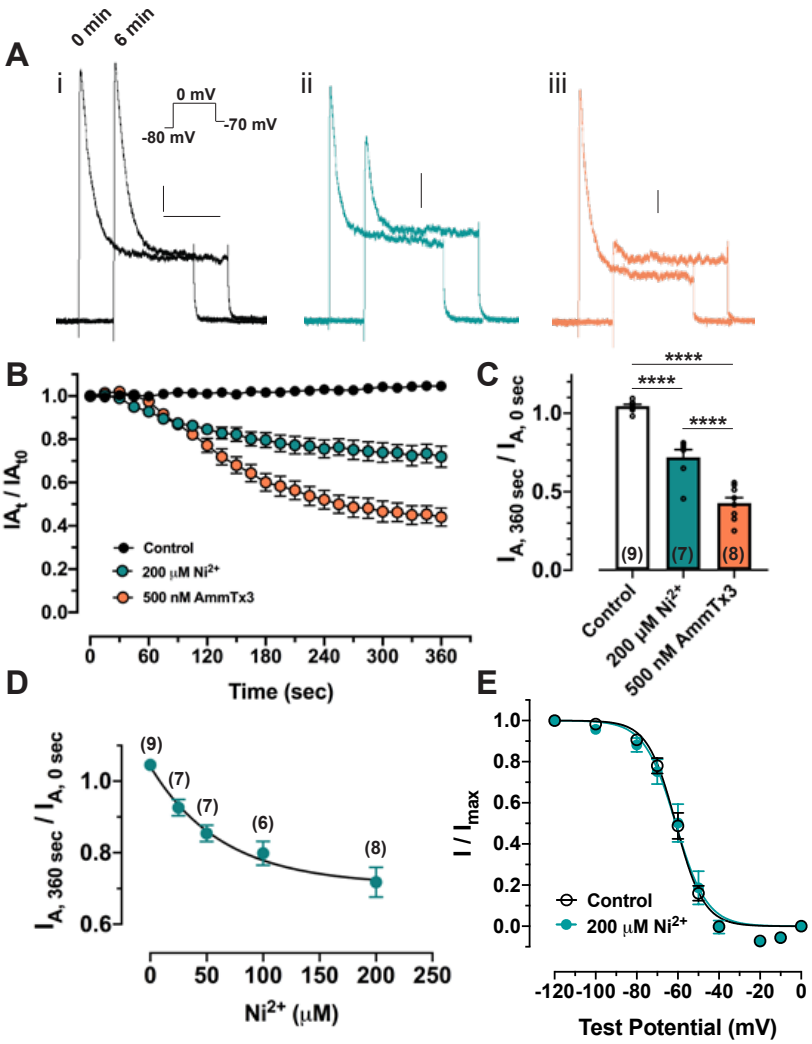

Figure 5. Cav2.3 sustains I_A in cultured hippocampal neurons.

A. Representative traces from whole-cell voltage clamp time courses for untreated neurons (i), and those treated with either Ni^{2+} (ii, 200 μM) or AmmTx3 (iii, 500 nM). First and last traces in the 6 min time course are shown superimposed with the final trace nudged 100 ms to the right. y-scale = 200 pA, x-scale = 200 ms. **B.** Averaged peak outward current normalized to current at break-in is plotted against the duration of the experiment. Drug wash-in began at 15 s. **C.** Outward current remaining at the end of the recording period was normalized to current at break-in and plotted for each condition. Cell numbers from 1-2 cultures are indicated within parentheses. **D.** Reduction in outward current was plotted for a range of Ni^{2+} concentrations. Averages at each concentration of Ni^{2+} were fit to a single exponential function. Cell numbers from 2 cultures are indicated within parentheses. **E.** Voltage-dependence of inactivation is plotted as the peak outward current elicited from a range of conditioning test potentials. Error bars represent +/- SEM

of 4 (control) or 7 (Ni^{2+}) cells from 1 culture. **** $p < 0.0001$. Statistical significance was evaluated by one-way ANOVA with Tukey's multiple comparisons test.

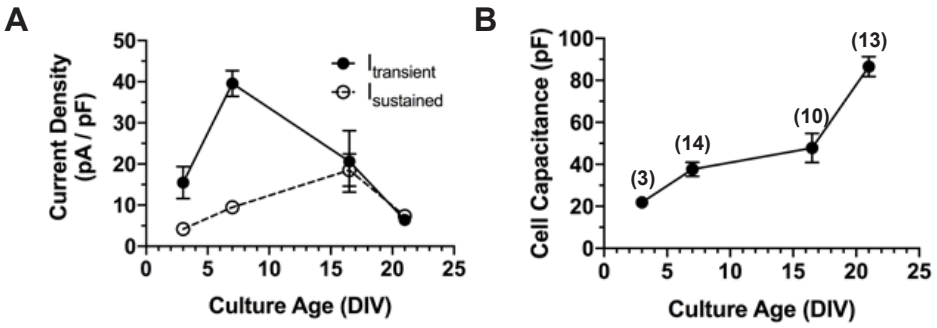

Figure 5 – Figure Supplement 1. Somatic I_A current density peaks early in developing cultured hippocampal neurons

A. Mean transient and sustained currents plotted by neuronal age in culture. **B.** Cell size measured by capacitance on break-in is plotted by neuronal age in culture. Number of cells are indicated in parentheses for **A** and **B**. Error bars represent +/- SEM from 1-2 cultures.

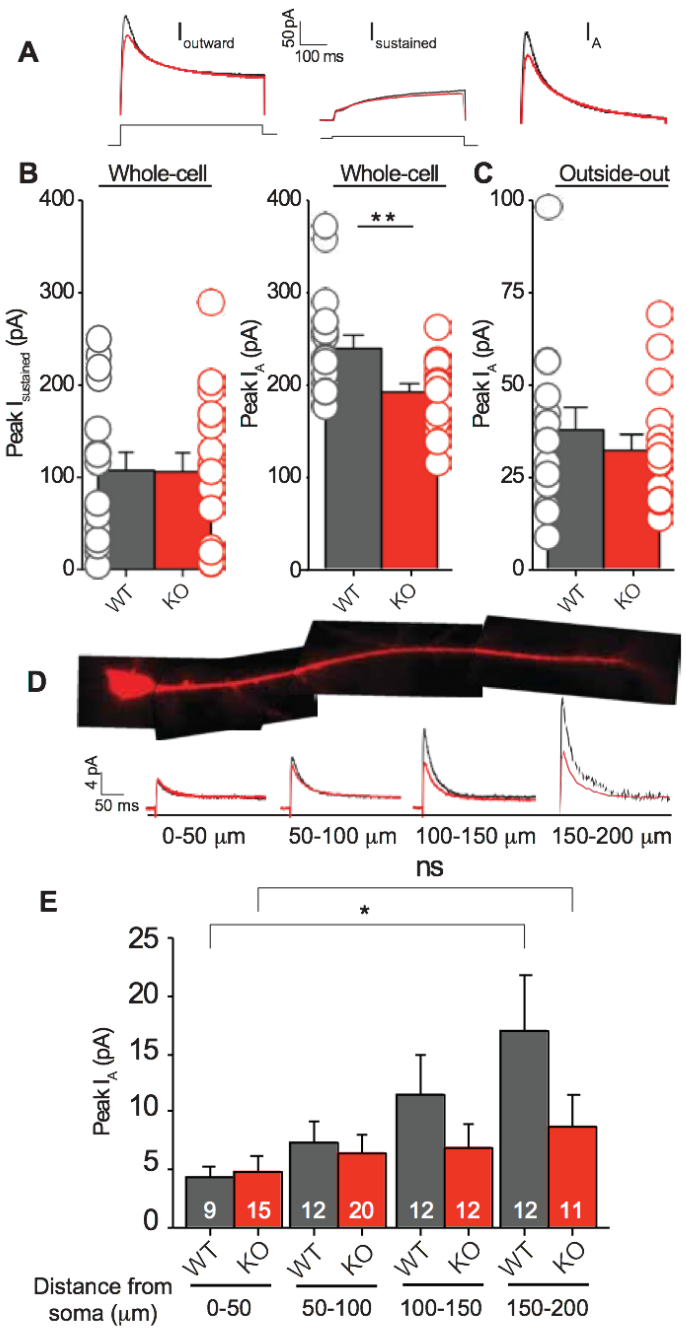

Figure 6. I_A is reduced in Cav2.3 KO CA1 pyramidal neurons.

A. Representative traces for total outward current, sustained current, and isolated I_A from the soma of WT or Cav2.3 KO mouse CA1 pyramidal neurons. **B.** Bar graphs compare the mean sustained and isolated I_A amplitude in WT and Cav2.3 KO mouse neuronal soma. n = 17 WT and 16 KO cells. **C.** Comparison of I_A in outside-out patches from the neuronal soma of WT and Cav2.3 KO. n = 14 WT and 15 KO cells. **D.** Above, a representative CA1 pyramidal neuron and apical dendrite made visible by Alexa 594 dye in the patch pipette. Below, representative cell-attached

recordings from the apical dendrites of WT and Cav2.3 KO neurons at various distances from the neuronal cell body. **E.** I_A is plotted for dendrite segments. The I_A gradient is dramatically reduced in Cav2.3 KO dendrites relative to WT. Parentheses indicate number of patches included in analysis. Error bars represent +/- SEM. ns = not statistically significant, * $p < 0.05$, ** $p < 0.01$. Statistical significance was evaluated by either student's t-test (**B**) or one-way ANOVA with Tukey's multiple comparisons test (**E**).

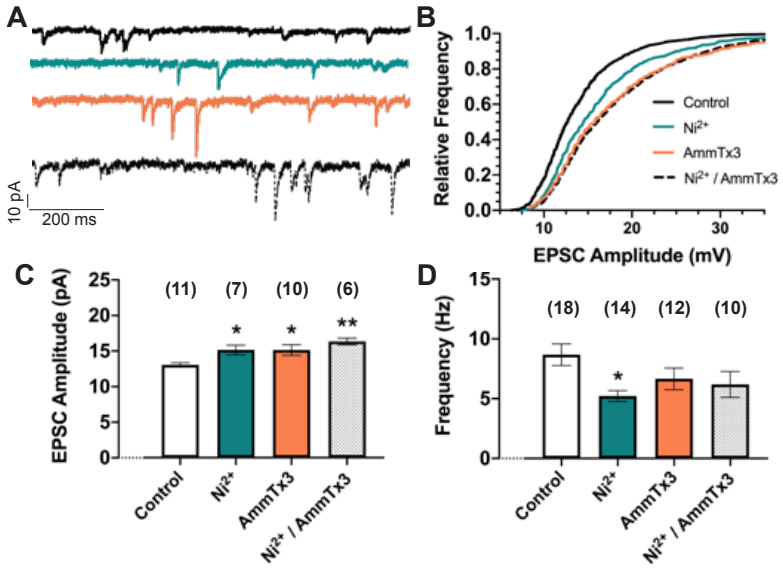

Figure 7. R-type Ca^{2+} channels regulate I_A attenuation of AMPAR-mediate mEPSCs.

A. Representative traces of miniature excitatory postsynaptic potentials measured from cultured hippocampal neurons at -70 mV in the absence and presence of Ni^{2+} or AmmTx3. **B.** The relative frequency distribution of mEPSCs are plotted against amplitude. Distribution of mEPSCs in the presence of Ni^{2+}, AmmTx3, or Ni^{2+} and AmmTx3 in combination are shifted toward a higher proportion of larger events. Analysis includes 638-1685 events **C.** Median mEPSC amplitudes are plotted for each condition recorded in **B**. Parentheses indicate cell numbers from 5 cultures. AmmTx3 increases median amplitude as does Ni^{2+} and AmmTx3 in combination. **D.** mEPSC frequency is decreased in the presence of Ni^{2+}, likely due to effects on presynaptic voltage-gated Ca^{2+} channels. Parentheses indicate cell numbers from 5 cultures. Error bars represent +/- SEM. * $p < 0.05$, ** $p < 0.01$. Statistical significance was evaluated by one-way ANOVA with Tukey's multiple comparisons test.

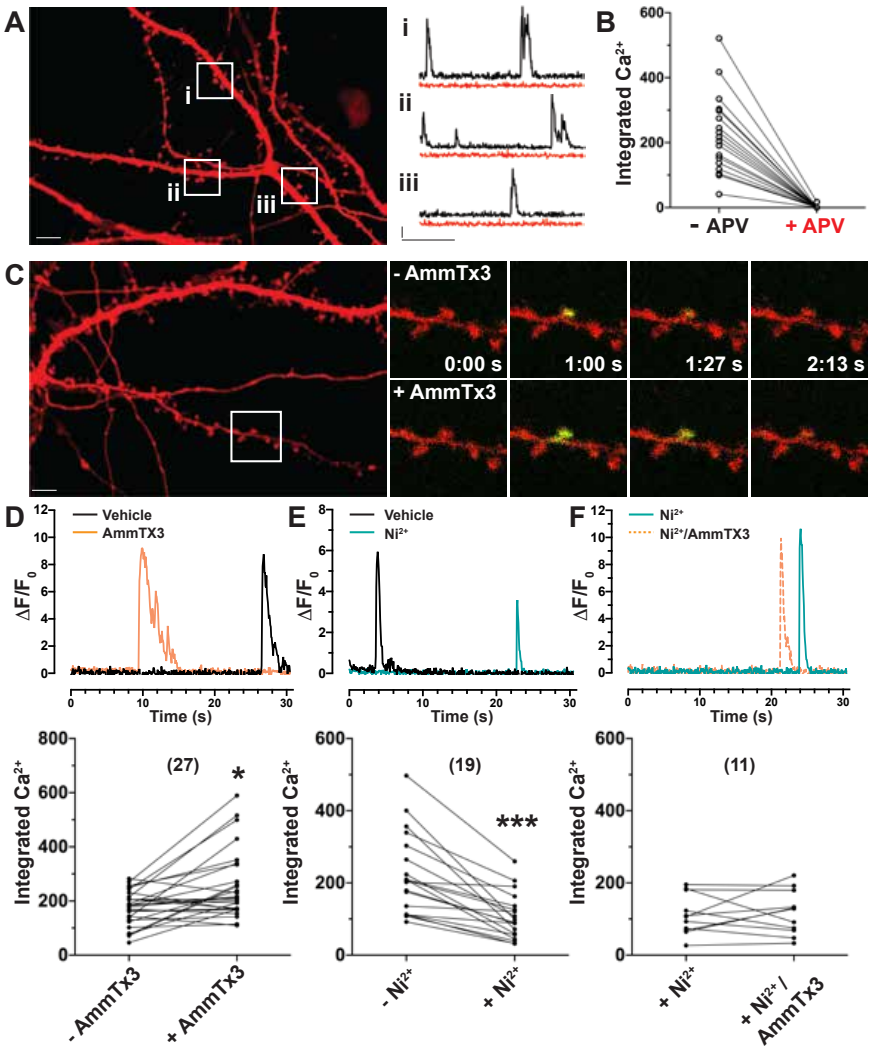

Figure 8. R-type Ca^{2+} channels regulate I_A attenuation of NMDAR-mediated spine Ca^{2+} influx.

A. Left, A representative neuron expressing mCherry (red) and GCaMP6f (not shown). Three representative spines (i, ii, and iii) were chosen to demonstrate typical spontaneous spine Ca^{2+} transients in the panel at right. Scale bar: 5 μm. Right, Traces plot the magnitude of GCaMP6f fluorescence ($\Delta F/F_0$) over time for each representative spine before (black traces) and after a 10 min application of D-APV (50 μM) (red traces). Scale bar: y = 2 $\Delta F/F_0$; x = 10 s. **B.** The integral of each Ca^{2+} transient for many spines is plotted before and after application of D-APV application demonstrating the NMDAR-dependence under these conditions. **C.** Left, A neuron transfected as in A, but treated with the Kv4 channel antagonist AmmTx3 (500 nM). Right, timelapse images of a representative spine before (above) and after (below) AmmTx3 treatment. **D.** Above, the magnitude of GCaMP6f fluorescence ($\Delta F/F_0$) over time in a single representative spine is plotted

for each drug treatment. Below, integrated Ca^{2+} influx is plotted for many spines before and after the indicated conditions. Spine numbers from 2-4 cultures are indicated in parentheses. Only spines with at least one event before and after treatments were included in the analysis. * $p < 0.05$, *** $p < 0.001$. Statistical significance was evaluated by two-way ANOVA with Sidak's multiple comparisons test.

REFERENCES

1. Maletic-Savatic M, Lenn NJ, Trimmer JS. Differential spatiotemporal expression of K+ channel polypeptides in rat hippocampal neurons developing in situ and in vitro. J Neurosci. 1995;15(5 Pt 2):3840-51.
2. Sheng M, Tsaur ML, Jan YN, Jan LY. Subcellular segregation of two A-type K+ channel proteins in rat central neurons. Neuron. 1992;9(2):271-84.
3. Serodio P, Rudy B. Differential expression of Kv4 K+ channel subunits mediating subthreshold transient K+ (A-type) currents in rat brain. J Neurophysiol. 1998;79(2):1081-91.
4. Ramakers GM, Storm JF. A postsynaptic transient K(+) current modulated by arachidonic acid regulates synaptic integration and threshold for LTP induction in hippocampal pyramidal cells. Proc Natl Acad Sci U S A. 2002;99(15):10144-9.
5. Hoffman DA, Magee JC, Colbert CM, Johnston D. K+ channel regulation of signal propagation in dendrites of hippocampal pyramidal neurons. Nature. 1997;387(6636):869-75.
6. Gasparini S, Losonczy A, Chen X, Johnston D, Magee JC. Associative pairing enhances action potential back-propagation in radial oblique branches of CA1 pyramidal neurons. J Physiol. 2007;580(Pt.3):787-800.
7. Cai X, Liang CW, Muralidharan S, Kao JP, Tang CM, Thompson SM. Unique roles of SK and Kv4.2 potassium channels in dendritic integration. Neuron. 2004;44(2):351-64.
8. Kim J, Wei DS, Hoffman DA. Kv4 potassium channel subunits control action potential repolarization and frequency-dependent broadening in rat hippocampal CA1 pyramidal neurones. J Physiol. 2005;569(Pt 1):41-57.
9. Seong HJ, Behnia R, Carter AG. Impact of subthreshold membrane potential on synaptic responses at dendritic spines of layer 5 pyramidal neurons in the prefrontal cortex. J Neurophysiol. 2014;111(10):1960-72.
10. Cash S, Yuste R. Input summation by cultured pyramidal neurons is linear and position-independent. J Neurosci. 1998;18(1):10-5.
11. Cash S, Yuste R. Linear summation of excitatory inputs by CA1 pyramidal neurons. Neuron. 1999;22(2):383-94.
12. Watanabe S, Hoffman DA, Migliore M, Johnston D. Dendritic K+ channels contribute to spike-timing dependent long-term potentiation in hippocampal pyramidal neurons. Proc Natl Acad Sci U S A. 2002;99(12):8366-71.
13. Chen X, Yuan LL, Zhao C, Birnbaum SG, Frick A, Jung WE, et al. Deletion of Kv4.2 gene eliminates dendritic A-type K+ current and enhances induction of long-term potentiation in hippocampal CA1 pyramidal neurons. J Neurosci. 2006;26(47):12143-51.

14. Lockridge A, Yuan LL. Spatial learning deficits in mice lacking A-type K(+) channel subunits. Hippocampus. 2011;21(11):1152-6.
15. Sun W, Maffie JK, Lin L, Petralia RS, Rudy B, Hoffman DA. DPP6 establishes the A-type K(+) current gradient critical for the regulation of dendritic excitability in CA1 hippocampal neurons. Neuron. 2011;71(6):1102-15.
16. Wang HG, He XP, Li Q, Madison RD, Moore SD, McNamara JO, et al. The auxiliary subunit KChIP2 is an essential regulator of homeostatic excitability. J Biol Chem. 2013;288(19):13258-68.
17. Andrasfalvy BK, Makara JK, Johnston D, Magee JC. Altered synaptic and non-synaptic properties of CA1 pyramidal neurons in Kv4.2 knockout mice. J Physiol. 2008;586(16):3881-92.
18. Locke RE, Nerbonne JM. Role of voltage-gated K+ currents in mediating the regular-spiking phenotype of callosal-projecting rat visual cortical neurons. J Neurophysiol. 1997;78(5):2321-35.
19. Singh B, Ogiwara I, Kaneda M, Tokonami N, Mazaki E, Baba K, et al. A Kv4.2 truncation mutation in a patient with temporal lobe epilepsy. Neurobiol Dis. 2006;24(2):245-53.
20. Gross C, Yao X, Engel T, Tiwari D, Xing L, Rowley S, et al. MicroRNA-Mediated Downregulation of the Potassium Channel Kv4.2 Contributes to Seizure Onset. Cell Rep. 2016;17(1):37-45.
21. Tiwari D, Brager DH, Rymer JK, Bunk AT, White AR, Elsayed NA, et al. MicroRNA inhibition upregulates hippocampal A-type potassium current and reduces seizure frequency in a mouse model of epilepsy. Neurobiol Dis. 2019;130:104508.
22. Barnwell LF, Lugo JN, Lee WL, Willis SE, Gertz SJ, Hrachovy RA, et al. Kv4.2 knockout mice demonstrate increased susceptibility to convulsant stimulation. Epilepsia. 2009;50(7):1741-51.
23. Bernard C, Anderson A, Becker A, Poolos NP, Beck H, Johnston D. Acquired dendritic channelopathy in temporal lobe epilepsy. Science. 2004;305(5683):532-5.
24. Monaghan MM, Menegola M, Vacher H, Rhodes KJ, Trimmer JS. Altered expression and localization of hippocampal A-type potassium channel subunits in the pilocarpine-induced model of temporal lobe epilepsy. Neuroscience. 2008;156(3):550-62.
25. Hall AM, Throesch BT, Buckingham SC, Markwardt SJ, Peng Y, Wang Q, et al. Tau-dependent Kv4.2 depletion and dendritic hyperexcitability in a mouse model of Alzheimer's disease. J Neurosci. 2015;35(15):6221-30.
26. Zemel BM, Ritter DM, Covarrubias M, Muqeem T. A-Type KV Channels in Dorsal Root Ganglion Neurons: Diversity, Function, and Dysfunction. Front Mol Neurosci. 2018;11:253.
27. An WF, Bowlby MR, Betty M, Cao J, Ling HP, Mendoza G, et al. Modulation of A-type potassium channels by a family of calcium sensors. Nature. 2000;403(6769):553-6.
28. Nadal MS, Ozaita A, Amarillo Y, Vega-Saenz de Miera E, Ma Y, Mo W, et al. The CD26-related dipeptidyl aminopeptidase-like protein DPPX is a critical component of neuronal A-type K+ channels. Neuron. 2003;37(3):449-61.
29. Lin L, Sun W, Wikenheiser AM, Kung F, Hoffman DA. KChIP4a regulates Kv4.2 channel trafficking through PKA phosphorylation. Mol Cell Neurosci. 2010;43(3):315-25.
30. Foeger NC, Marionneau C, Nerbonne JM. Co-assembly of Kv4 {alpha} subunits with K+ channel-interacting protein 2 stabilizes protein expression and promotes surface retention of channel complexes. J Biol Chem. 2010;285(43):33413-22.

1152 31. Pioletti M, Findeisen F, Hura GL, Minor DL, Jr. Three-dimensional structure of the
1153 KChIP1-Kv4.3 T1 complex reveals a cross-shaped octamer. Nat Struct Mol Biol. 2006;13(11):987-
1154 95.
1155 32. Wang H, Yan Y, Liu Q, Huang Y, Shen Y, Chen L, et al. Structural basis for modulation of
1156 Kv4 K+ channels by auxiliary KChIP subunits. Nat Neurosci. 2007;10(1):32-9.
1157 33. Jerng HH, Pfaffinger PJ. Modulatory mechanisms and multiple functions of
1158 somatodendritic A-type K (+) channel auxiliary subunits. Front Cell Neurosci. 2014;8:82.
1159 34. Burgoyne RD. Neuronal calcium sensor proteins: generating diversity in neuronal Ca2+
1160 signalling. Nat Rev Neurosci. 2007;8(3):182-93.
1161 35. Lee L, Chen KC, Chang LS. Functional roles of EF-hands in human potassium channel-
1162 interacting protein 2.2. Protein Pept Lett. 2009;16(9):1081-7.
1163 36. Craig TA, Benson LM, Venyaminov SY, Klimtchuk ES, Bajzer Z, Prendergast FG, et al. The
1164 metal-binding properties of DREAM: evidence for calcium-mediated changes in DREAM
1165 structure. J Biol Chem. 2002;277(13):10955-66.
1166 37. Osawa M, Tong KI, Lilliehook C, Wasco W, Buxbaum JD, Cheng HY, et al. Calcium-
1167 regulated DNA binding and oligomerization of the neuronal calcium-sensing protein,
1168 calsenilin/DREAM/KChIP3. J Biol Chem. 2001;276(44):41005-13.
1169 38. Lin YL, Chen CY, Cheng CP, Chang LS. Protein-protein interactions of KChIP proteins and
1170 Kv4.2. Biochem Biophys Res Commun. 2004;321(3):606-10.
1171 39. Gonzalez WG, Pham K, Miksovska J. Modulation of the voltage-gated potassium channel
1172 (Kv4.3) and the auxiliary protein (KChIP3) interactions by the current activator NS5806. J Biol
1173 Chem. 2014;289(46):32201-13.
1174 40. Morohashi Y, Hatano N, Ohya S, Takikawa R, Watabiki T, Takasugi N, et al. Molecular
1175 cloning and characterization of CALP/KChIP4, a novel EF-hand protein interacting with
1176 presenilin 2 and voltage-gated potassium channel subunit Kv4. J Biol Chem.
1177 2002;277(17):14965-75.
1178 41. Groen C, Bahring R. Modulation of human Kv4.3/KChIP2 channel inactivation kinetics by
1179 cytoplasmic Ca(2). Pflugers Arch. 2017;469(11):1457-70.
1180 42. Murphy JG, Hoffman DA. A polybasic motif in alternatively spliced KChIP2 isoforms
1181 prevents Ca(2+) regulation of Kv4 channels. J Biol Chem. 2019;294(10):3683-95.
1182 43. Osawa M, Dace A, Tong KI, Valiveti A, Ikura M, Ames JB. Mg2+ and Ca2+ differentially
1183 regulate DNA binding and dimerization of DREAM. J Biol Chem. 2005;280(18):18008-14.
1184 44. Chen QX, Wong RK. Intracellular Ca2+ suppressed a transient potassium current in
1185 hippocampal neurons. J Neurosci. 1991;11(2):337-43.
1186 45. Wang X, Bao J, Zeng XM, Liu Z, Mei YA. Elevation of intracellular Ca2+ modulates A-
1187 currents in rat cerebellar granule neurons. J Neurosci Res. 2005;81(4):530-40.
1188 46. Patel SP, Campbell DL, Strauss HC. Elucidating KChIP effects on Kv4.3 inactivation and
1189 recovery kinetics with a minimal KChIP2 isoform. J Physiol. 2002;545(1):5-11.
1190 47. Vergara C, Latorre R, Marrion NV, Adelman JP. Calcium-activated potassium channels.
1191 Curr Opin Neurobiol. 1998;8(3):321-9.
1192 48. Anderson D, Rehak R, Hameed S, Mehaffey WH, Zamponi GW, Turner RW. Regulation of
1193 the KV4.2 complex by CaV3.1 calcium channels. Channels (Austin). 2010;4(3):163-7.
1194 49. Anderson D, Mehaffey WH, Iftinca M, Rehak R, Engbers JD, Hameed S, et al. Regulation
1195 of neuronal activity by Cav3-Kv4 channel signaling complexes. Nat Neurosci. 2010;13(3):333-7.

50. Wang K, Lin MT, Adelman JP, Maylie J. Distinct Ca2+ sources in dendritic spines of hippocampal CA1 neurons couple to SK and Kv4 channels. Neuron. 2014;81(2):379-87.
51. Parajuli LK, Nakajima C, Kulik A, Matsui K, Schneider T, Shigemoto R, et al. Quantitative regional and ultrastructural localization of the Ca(v)2.3 subunit of R-type calcium channel in mouse brain. J Neurosci. 2012;32(39):13555-67.
52. Sabatini BL, Svoboda K. Analysis of calcium channels in single spines using optical fluctuation analysis. Nature. 2000;408(6812):589-93.
53. Magee JC, Johnston D. Characterization of single voltage-gated Na+ and Ca2+ channels in apical dendrites of rat CA1 pyramidal neurons. J Physiol. 1995;487(1):67-90.
54. Metz AE, Jarsky T, Martina M, Spruston N. R-type calcium channels contribute to afterdepolarization and bursting in hippocampal CA1 pyramidal neurons. J Neurosci. 2005;25(24):5763-73.
55. Bloodgood BL, Sabatini BL. Nonlinear regulation of unitary synaptic signals by CaV(2.3) voltage-sensitive calcium channels located in dendritic spines. Neuron. 2007;53(2):249-60.
56. Takahashi H, Magee JC. Pathway interactions and synaptic plasticity in the dendritic tuft regions of CA1 pyramidal neurons. Neuron. 2009;62(1):102-11.
57. Gutzmann JJ, Lin L, Hoffman DA. Functional Coupling of Cav2.3 and BK Potassium Channels Regulates Action Potential Repolarization and Short-Term Plasticity in the Mouse Hippocampus. Front Cell Neurosci. 2019;13:27.
58. Hu JH, Malloy C, Tabor GT, Gutzmann JJ, Liu Y, Abebe D, et al. Activity-dependent isomerization of Kv4.2 by Pin1 regulates cognitive flexibility. Nat Commun. 2020;11(1):1567.
59. Rhodes KJ, Carroll KI, Sung MA, Doliveira LC, Monaghan MM, Burke SL, et al. KChIPs and Kv4 alpha subunits as integral components of A-type potassium channels in mammalian brain. J Neurosci. 2004;24(36):7903-15.
60. Wong W, Newell EW, Jugloff DG, Jones OT, Schlichter LC. Cell surface targeting and clustering interactions between heterologously expressed PSD-95 and the Shal voltage-gated potassium channel, Kv4.2. J Biol Chem. 2002;277(23):20423-30.
61. Hammond RS, Lin L, Sidorov MS, Wikenheiser AM, Hoffman DA. Protein kinase a mediates activity-dependent Kv4.2 channel trafficking. J Neurosci. 2008;28(30):7513-9.
62. Gardoni F, Mauceri D, Marcello E, Sala C, Di Luca M, Jeromin A. SAP97 directs the localization of Kv4.2 to spines in hippocampal neurons: regulation by CaMKII. J Biol Chem. 2007;282(39):28691-9.
63. Lin L, Sun W, Kung F, Dell'Acqua ML, Hoffman DA. AKAP79/150 impacts intrinsic excitability of hippocampal neurons through phospho-regulation of A-type K+ channel trafficking. J Neurosci. 2011;31(4):1323-32.
64. Förster T. Zwischenmolekulare Energiewanderung und Fluoreszenz. Annalen der Physik. 1948;437:55-75.
65. Lakowicz JR. Principles of fluorescence spectroscopy. 3rd ed. New York: Springer; 2006. xxvi, 954 p. p.
66. Ben-Johny M, Yue DN, Yue DT. Detecting stoichiometry of macromolecular complexes in live cells using FRET. Nat Commun. 2016;7:13709.
67. Naraghi M, Neher E. Linearized buffered Ca2+ diffusion in microdomains and its implications for calculation of [Ca2+] at the mouth of a calcium channel. J Neurosci. 1997;17(18):6961-73.

1240 68. Augustine GJ, Santamaria F, Tanaka K. Local calcium signaling in neurons. Neuron.
1241 2003;40(2):331-46.
1242 69. Gray EE, Murphy JG, Liu Y, Trang I, Tabor GT, Lin L, et al. Disruption of GpI mGluR-
1243 Dependent Cav2.3 Translation in a Mouse Model of Fragile X Syndrome. J Neurosci.
1244 2019;39(38):7453-64.
1245 70. Soong TW, Stea A, Hodson CD, Dubel SJ, Vincent SR, Snutch TP. Structure and functional
1246 expression of a member of the low voltage-activated calcium channel family. Science.
1247 1993;260(5111):1133-6.
1248 71. Maffie JK, Dvoretskova E, Bougis PE, Martin-Eauclaire MF, Rudy B. Dipeptidyl-peptidase-
1249 like-proteins confer high sensitivity to the scorpion toxin AmmTX3 to Kv4-mediated A-type K+
1250 channels. J Physiol. 2013;591(10):2419-27.
1251 72. Vacher H, Alami M, Crest M, Possani LD, Bougis PE, Martin-Eauclaire MF. Expanding the
1252 scorpion toxin alpha-KTX 15 family with AmmTX3 from Androctonus mauretanicus. Eur J
1253 Biochem. 2002;269(24):6037-41.
1254 73. Myoga MH, Regehr WG. Calcium microdomains near R-type calcium channels control
1255 the induction of presynaptic long-term potentiation at parallel fiber to purkinje cell synapses. J
1256 Neurosci. 2011;31(14):5235-43.
1257 74. Williams ME, Marubio LM, Deal CR, Hans M, Brust PF, Philipson LH, et al. Structure and
1258 functional characterization of neuronal alpha 1E calcium channel subtypes. J Biol Chem.
1259 1994;269(35):22347-57.
1260 75. Wilson SM, Toth PT, Oh SB, Gillard SE, Volsen S, Ren D, et al. The status of voltage-
1261 dependent calcium channels in alpha 1E knock-out mice. J Neurosci. 2000;20(23):8566-71.
1262 76. Magee JC, Christofi G, Miyakawa H, Christie B, Lasser-Ross N, Johnston D. Subthreshold
1263 synaptic activation of voltage-gated Ca2+ channels mediates a localized Ca2+ influx into the
1264 dendrites of hippocampal pyramidal neurons. J Neurophysiol. 1995;74(3):1335-42.
1265 77. Grunditz A, Holbro N, Tian L, Zuo Y, Oertner TG. Spine neck plasticity controls
1266 postsynaptic calcium signals through electrical compartmentalization. J Neurosci.
1267 2008;28(50):13457-66.
1268 78. Kerti K, Lorincz A, Nusser Z. Unique somato-dendritic distribution pattern of Kv4.2
1269 channels on hippocampal CA1 pyramidal cells. Eur J Neurosci. 2012;35(1):66-75.
1270 79. Wang K, Kelley MH, Wu WW, Adelman JP, Maylie J. Apamin Boosting of Synaptic
1271 Potentials in CaV2.3 R-Type Ca2+ Channel Null Mice. PLoS One. 2015;10(9):e0139332.
1272 80. Bloodgood BL, Giessel AJ, Sabatini BL. Biphasic synaptic Ca influx arising from
1273 compartmentalized electrical signals in dendritic spines. PLoS Biol. 2009;7(9):e1000190.
1274 81. Kim J, Jung S, Clemens A, Petralia R, Hoffman DA. Regulation of Dendritic Excitability by
1275 Activity-Dependent Trafficking of the A-Type K+ Channel Subunit Kv4.2 in Hippocampal
1276 Neurons. Neuron. 2007;54(6):933-47.
1277 82. Gasparini S, Kasyanov AM, Pietrobon D, Voronin LL, Cherubini E. Presynaptic R-type
1278 calcium channels contribute to fast excitatory synaptic transmission in the rat hippocampus. J
1279 Neurosci. 2001;21(22):8715-21.
1280 83. Sinnen BL, Bowen AB, Gibson ES, Kennedy MJ. Local and Use-Dependent Effects of beta-
1281 Amyloid Oligomers on NMDA Receptor Function Revealed by Optical Quantal Analysis. J
1282 Neurosci. 2016;36(45):11532-43.

84. Murthy VN, Sejnowski TJ, Stevens CF. Dynamics of dendritic calcium transients evoked by quantal release at excitatory hippocampal synapses. Proc Natl Acad Sci U S A. 2000;97(2):901-6.
85. Reese AL, Kavalali ET. Spontaneous neurotransmission signals through store-driven Ca(2+) transients to maintain synaptic homeostasis. Elife. 2015;4.
86. Shah MM, Hammond RS, Hoffman DA. Dendritic ion channel trafficking and plasticity. Trends Neurosci. 2010;33(7):307-16.
87. Stuart G, Spruston N, Häusser M. Dendrites. Third edition. ed. Oxford ;: Oxford University Press; 2016. xxi, 714 pages p.
88. Johnston D, Christie BR, Frick A, Gray R, Hoffman DA, Schexnayder LK, et al. Active dendrites, potassium channels and synaptic plasticity. Philos Trans R Soc Lond B Biol Sci. 2003;358(1432):667-74.
89. Kimm T, Bean BP. Inhibition of A-type potassium current by the peptide toxin SNX-482. J Neurosci. 2014;34(28):9182-9.
90. Newcomb R, Szoke B, Palma A, Wang G, Chen X, Hopkins W, et al. Selective peptide antagonist of the class E calcium channel from the venom of the tarantula Hysterocrates gigas. Biochemistry. 1998;37(44):15353-62.
91. Long SB, Campbell EB, Mackinnon R. Crystal structure of a mammalian voltage-dependent Shaker family K+ channel. Science. 2005;309(5736):897-903.
92. Zhou W, Qian Y, Kunjilwar K, Pfaffinger PJ, Choe S. Structural insights into the functional interaction of KChIP1 with Shal-type K(+) channels. Neuron. 2004;41(4):573-86.
93. Scannevin RH, Wang K, Jow F, Megules J, Kopsco DC, Edris W, et al. Two N-terminal domains of Kv4 K(+) channels regulate binding to and modulation by KChIP1. Neuron. 2004;41(4):587-98.
94. Walker AS, Neves G, Grillo F, Jackson RE, Rigby M, O'Donnell C, et al. Distance-dependent gradient in NMDAR-driven spine calcium signals along tapering dendrites. Proc Natl Acad Sci U S A. 2017;114(10):E1986-E95.
95. Metzbower SR, Joo Y, Benavides DR, Blanpied TA. Properties of Individual Hippocampal Synapses Influencing NMDA-Receptor Activation by Spontaneous Neurotransmission. eNeuro. 2019;6(3).
96. Jung SC, Hoffman DA. Biphasic somatic A-type K channel downregulation mediates intrinsic plasticity in hippocampal CA1 pyramidal neurons. PLoS One. 2009;4(8):e6549.
97. Holmqvist MH, Cao J, Hernandez-Pineda R, Jacobson MD, Carroll KI, Sung MA, et al. Elimination of fast inactivation in Kv4 A-type potassium channels by an auxiliary subunit domain. Proc Natl Acad Sci U S A. 2002;99(2):1035-40.
98. Beck EJ, Bowlby M, An WF, Rhodes KJ, Covarrubias M. Remodelling inactivation gating of Kv4 channels by KChIP1, a small-molecular-weight calcium-binding protein. J Physiol. 2002;538(Pt 3):691-706.
99. Kunjilwar K, Qian Y, Pfaffinger PJ. Functional stoichiometry underlying KChIP regulation of Kv4.2 functional expression. J Neurochem. 2013;126(4):462-72.
100. Zhou J, Tang Y, Zheng Q, Li M, Yuan T, Chen L, et al. Different KChIPs compete for heteromultimeric assembly with pore-forming Kv4 subunits. Biophys J. 2015;108(11):2658-69.

101. Kitazawa M, Kubo Y, Nakajo K. The stoichiometry and biophysical properties of the Kv4 potassium channel complex with K+ channel-interacting protein (KChIP) subunits are variable, depending on the relative expression level. J Biol Chem. 2014;289(25):17597-609.
102. Varga AW, Anderson AE, Adams JP, Vogel H, Sweatt JD. Input-specific immunolocalization of differentially phosphorylated Kv4.2 in the mouse brain. Learn Mem. 2000;7(5):321-32.
103. Yuan LL, Adams JP, Swank M, Sweatt JD, Johnston D. Protein kinase modulation of dendritic K+ channels in hippocampus involves a mitogen-activated protein kinase pathway. J Neurosci. 2002;22(12):4860-8.
104. Hoffman DA, Johnston D. Downregulation of transient K+ channels in dendrites of hippocampal CA1 pyramidal neurons by activation of PKA and PKC. J Neurosci. 1998;18(10):3521-8.
105. Patriarchi T, Buonarati OR, Hell JW. Postsynaptic localization and regulation of AMPA receptors and Cav1.2 by beta2 adrenergic receptor/PKA and Ca(2+)/CaMKII signaling. EMBO J. 2018;37(20).
106. Jerng HH, Pfaffinger PJ. Multiple Kv channel-interacting proteins contain an N-terminal transmembrane domain that regulates Kv4 channel trafficking and gating. J Biol Chem. 2008;283(51):36046-59.
107. Cajigas IJ, Tushev G, Will TJ, tom Dieck S, Fuerst N, Schuman EM. The local transcriptome in the synaptic neuropil revealed by deep sequencing and high-resolution imaging. Neuron. 2012;74(3):453-66.
108. Biever A, Glock C, Tushev G, Ciirdaeva E, Dalmay T, Langer JD, et al. Monosomes actively translate synaptic mRNAs in neuronal processes. Science. 2020;367(6477).
109. Massone S, Vassallo I, Castelnuovo M, Fiorino G, Gatta E, Robello M, et al. RNA polymerase III drives alternative splicing of the potassium channel-interacting protein contributing to brain complexity and neurodegeneration. J Cell Biol. 2011;193(5):851-66.
110. Schrader LA, Anderson AE, Mayne A, Pfaffinger PJ, Sweatt JD. PKA modulation of Kv4.2-encoded A-type potassium channels requires formation of a supramolecular complex. J Neurosci. 2002;22(23):10123-33.
111. Holmqvist MH, Cao J, Knoppers MH, Jurman ME, Distefano PS, Rhodes KJ, et al. Kinetic modulation of Kv4-mediated A-current by arachidonic acid is dependent on potassium channel interacting proteins. J Neurosci. 2001;21(12):4154-61.
112. Nicholson DA, Trana R, Katz Y, Kath WL, Spruston N, Geinisman Y. Distance-dependent differences in synapse number and AMPA receptor expression in hippocampal CA1 pyramidal neurons. Neuron. 2006;50(3):431-42.
113. Megias M, Emri Z, Freund TF, Gulyas AI. Total number and distribution of inhibitory and excitatory synapses on hippocampal CA1 pyramidal cells. Neuroscience. 2001;102(3):527-40.
114. Ulbrich MH, Isacoff EY. Subunit counting in membrane-bound proteins. Nat Methods. 2007;4(4):319-21.
115. Kremers GJ, Goedhart J, van den Heuvel DJ, Gerritsen HC, Gadella TW, Jr. Improved green and blue fluorescent proteins for expression in bacteria and mammalian cells. Biochemistry. 2007;46(12):3775-83.
116. Chen TW, Wardill TJ, Sun Y, Pulver SR, Renninger SL, Baohan A, et al. Ultrasensitive fluorescent proteins for imaging neuronal activity. Nature. 2013;499(7458):295-300.

117. Petralia RS, Wang YX, Hua F, Yi Z, Zhou A, Ge L, et al. Organization of NMDA receptors at extrasynaptic locations. Neuroscience. 2010;167(1):68-87.
118. Kaminski CF, Rees EJ, Schierle GS. A quantitative protocol for intensity-based live cell FRET imaging. Methods Mol Biol. 2014;1076:445-54.
119. Chen H, Puhl HL, 3rd, Koushik SV, Vogel SS, Ikeda SR. Measurement of FRET efficiency and ratio of donor to acceptor concentration in living cells. Biophys J. 2006;91(5):L39-41.
120. Hoppe A, Christensen K, Swanson JA. Fluorescence resonance energy transfer-based stoichiometry in living cells. Biophys J. 2002;83(6):3652-64.
121. Murphy JG, Crosby KC, Dittmer PJ, Sather WA, Dell'Acqua ML. AKAP79/150 recruits the transcription factor NFAT to regulate signaling to the nucleus by neuronal L-type Ca(2+) channels. Mol Biol Cell. 2019;30(14):1743-56.
122. Phair RD, Misteli T. High mobility of proteins in the mammalian cell nucleus. Nature. 2000;404(6778):604-9.